

Chapter 2

State of the Art in the Characterization of Nano- and Atomic-Scale Catalysts

Devika Laishram, Divya Kumar, Unnati Gupta, R. Krishnapriya, and Rakesh K. Sharma*

Sustainable Materials and Catalysis Research Laboratory (SMCRL), Department of Chemistry, Indian Institute of Technology Jodhpur, Jodhpur, India 342037

*Email: rks@iitj.ac.in

Nanometer and subnanometer particles and films are becoming an essential and integral part of new technologies and inventions in different areas. Some of the most common areas include the microelectronic industry, magnetic recordings, photovoltaic applications, and optical coatings. Because of the ultrasmall size at atomic levels, the effect of quantum size becomes prominent, and the sensitivity of size is defined even by a difference of a single atom. Additionally, the effect is of utmost importance as the single-atom catalysts are far more advantageous than conventional catalysts as they tend to anchor easily because of their low coordination. Also, the presence of a single-atom catalyst in reactions creates efficient charge transfer as it forms a strong interaction with the support. Furthermore, catalysts in the subnanometer regime exhibit different electronic states and adsorption capabilities compared to traditional catalysts. Therefore, to fully appreciate the subnanometer catalysis reactions, it is essential to study the means of characterizing the prepared subnano catalysts, in order to characterize the materials in their as-synthesized form, to obtain a precise and accurate analysis; these are some of the fundamental requirements for achieving an optimum performance. The physical properties of many interesting materials for advanced technological usage are highly governed by the distribution and placement of atoms. Superior techniques such as high-resolution transmission electron microscopy and high-angle annular dark-field scanning transmission electron microscopy and infrared and X-ray absorption spectroscopic techniques provide electronic and geometric configurations and also reveal the transformation of the subnano catalysts on the support material. Modeling methods such as density functional theory can successfully predict the electronic structure and geometric configuration of the catalyst, which in turn influence the selectivity and activity of the catalyst. Thus, understanding the characterization techniques gives the ability to understand, identify, and measure the local environment of individual atoms and the interaction with the surface support, which will give fundamental knowledge and insights in the realms of nanoscience and technology, materials science, chemistry, and physics. Therefore, detection and enhanced measurement

of individual atoms is inherently challenging and is a prerequisite to the development of new technology and better performing materials. In this chapter, we have discussed various important methods of characterization for characterizing subnanometer and atomic catalysts.

Introduction

Nanomaterials and nanochemistry have evolved gigantically over the past few decades, especially in terms of synthesis, fabrication, characterization, and application in devices. This is a consequence of the extensive and exhaustive research that has been carried out, leading to a better understanding of the properties that the materials exhibit in the nano regime. Thus, size influenced the properties, and the occurrence of size-dependent phenomena such as quantum effects and surface plasmons can rationally be understood. Materials that earlier existed in bulk form can now be transformed into nanosized materials with enhanced properties, such as useful semiconductors (1), single-atom catalysts (2), transition metals (3), and noble metals (4). Other examples include the use of two-dimensional (2-D) materials such as graphene, which has revolutionized the world with its properties (5). When materials start existing as a single atom, then it represents the smallest quantum retaining the characteristics of the material via its local electronic environment (6).

In the field of heterogeneous catalysis, it is important to reduce the size of the catalyst and disperse it finely over a larger area of the support such as metal to improve the performance (7). Such a distribution impacts the use of its different active sites, affecting the selectivity. Thus, the size becomes the critical determining factor. It is vital to describe active centers for effective catalytic processes and high performance (8–10), and hence precision and control at the atomic level are necessary (9). Conventional systems of characterization, because of their inherent limitations in regards to accuracy and resolution, cannot be used to observe at the subnano level and other single-atom catalysts (11).

Therefore, new sensitive techniques need to be implemented to characterize, analyze, and understand these single and nano atom catalysts in order to effectively utilize them to their maximum potential. Additionally, due to their distinctive characteristics and behavior at the atomic level, the selectivity, activity, and stability change drastically. These single-atom catalysts offer more exposed reactive sites for catalytic reactions, unlike conventional nanoparticles, which suffer from excessive aggregation, leading to fewer exposed active sites.

The catalysts at the subnano level and single-atom catalysis have brought about high activity and selectivity in the field of heterogeneous catalysts. To fully understand and analyze these materials, many approaches have been established with the rapid advancement and development in characterization methods. Some of the characterization techniques discussed in this chapter include high-resolution scanning tunneling microscopy (STM), high-angle annular dark-field scanning transmission electron microscopy (HAADF-STEM), extended X-ray absorption fine structure (EXAFS), diffuse reflectance infrared Fourier transform spectroscopy (DRIFTS), X-ray photoelectron spectroscopy (XPS), NMR spectroscopy, and density functional theory (DFT) as a theoretical tool. The capacity to probe materials at the subnano level provides a huge understanding of the electronic structure and important chemical information and interaction of the molecules and the surface, which provide a deeper level of understanding of the atomic origins and their role in material properties.

Characterization Techniques

Electron Microscopy and Associated Techniques

Electron microscopy is instrumental for the characterization of a supported metal catalyst such as noble metal catalysts. It is an important tool for identifying the presence of single-atom catalysts from clusters or nanoparticles, especially for noble metals like Pt, Rh, and Pd. It is a powerful method for determining the spatial distribution of the single-atom catalysts and identifying the location of a single-atom catalyst in the support (6, 12). Furthermore, electron microscopy, along with associated techniques, can provide information such as the electronic state within the area of interest and other atomic-range information such as structure and morphology.

Qiao et al. (13) utilized aberration-corrected scanning transmission electron microscopy (STEM), having a sub-angstrom resolution, to identify and locate Pt atoms on the surface of an iron oxide (FeO_x) catalyst. The atomic-resolution HAADF provides enhanced contrast at low atomic numbers, unlike conventional TEM imaging, and also can identify the heavy atoms in the catalyst. The electrons scattered by the nuclei of the atom are detected using HAADF. The electrons are incoherent and quasi-elastic, mainly contributed by scattering at high angles of more than 80 mrad. Stroppa et al. (14) analyzed the three-dimensional morphology of faceted, nanocrystalline CeO_2 material using high-resolution scanning transmission electron microscopy (HAADF-HRSTEM). They were able to achieve this by determining the atomic column via a Gaussian mixture model (GMM), which is a parametric probability density function represented as a weighted sum of Gaussian component densities. The parameters of GMM are estimated using the iterative expectation-maximization algorithm or maximum a posteriori estimation from a well-trained prior model (15). In this work for the estimation of atomic column thickness, the integrated intensities were classified as a histogram, and the data-fitting procedure was carried out by using multiple normal distributions according to GMM (16). To optimize the model parameters, multiple runs of the GMM algorithm were performed. Later, each atomic column thickness was assigned to a Gaussian distribution (14), followed by identifying and assigning atomic positions using a crystallographic symmetric operation to construct the morphological model representation in three-dimensional (3-D) form. The HAADF-HRSTEM method of imaging is advantageous as it allows imaging of atomic columns directly at up to 50 pm resolution (17). The atomic number and the thickness of the atomic columns are measured from the intensity of the high-angle scattered electrons (18, 19). Thus, it allows reconstruction from an image or set of images of the nanocrystals by using crystallographic symmetry in combination with the HAADF intensity profile (20). However, there is still a limitation to the use of electron microscopy for determining 3-D structure, except for a few selected systems such as lightweight atoms having thin layers and specific Au clusters. For example, Figures 1a and 1b represent CeO_2 HAADF-HRSTEM images in which the atomic Ce columns are fairly distinguishable to be polyhedral and cubic-type nanocrystals. This is achieved by a combination of the electron imaging configuration and high-angle scattering of electrons, depending on the atomic weight. The Fourier transform (FT), inset of Figures 1a and 1b, establishes the atomic plane index and the orientation of the zonal axis (14). Additionally, HAADF-STEM gives information about the local chemistry and structure at the atomic level, which gives a comprehension of localization of single atoms. Ni atoms located on nanoporous graphene by substituting a carbon site in the carbon lattice provides stability of Ni atoms (21).

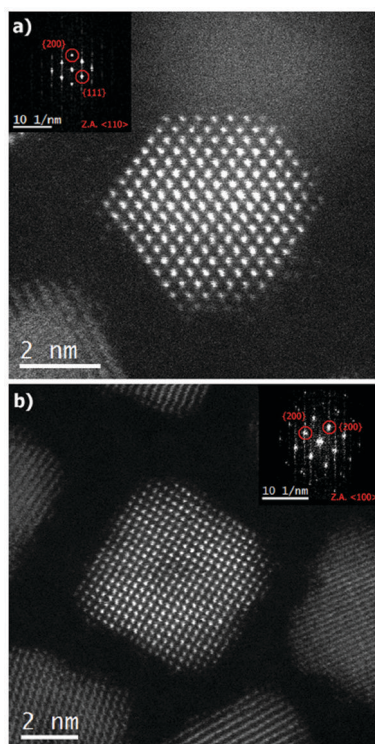


Figure 1. HAADF-HRSTEM images of CeO₂: (a) polyhedra and (b) cubic nanocrystals. The inset represents the FT images defining the zonal axes and the corresponding crystallographic planes. Reproduced with permission from ref. (14). Copyright 2013 Springer.

Li et al. (22) used HAADF STEM to locate the Pt atom distribution over a g-C₃N₄ support, where Pt atoms are uniformly dispersed, as confirmed by the bright spots. The existence of isolated Pt atoms was confirmed by the size of the Pt of less than 0.2 nm. However, with an increase in Pt loading, the spots become denser, implying the formation of subnanometer clusters of Pt. Similarly, Kumskov et al. (23) used a combination of HRSTEM and electron energy loss spectroscopy to identify the structure of a one-dimensional (1-D) unit cell of CuI nanocrystals having space group *Pm3m* inside single-walled carbon nanotubes (SWCNTs), as shown in Figure 2.

By simultaneously using both the dark and bright field modes of HRTEM, images can be observed with an enhanced contrast, such as in cases where small and drowned crystalline features need to be observed. Thus, rapidly developing technologies such as HAADF-STEM enable the study of metal atoms anchored on a structural support utilizing coordination with the center atom (24, 25). Additionally, researchers can understand the structural evolution dynamics of the nanosystem. Liu et al. (26) found that the evolution of Pt species and its stabilization on MCM-22 zeolites can be studied. Consequently, HAADF-STEM can be a highly functional and useful technique for exploring the dynamic interaction of metal and substrate and other changes such as oscillatory behavior and change in the shape of metal nanoparticles.

Thus, it can be concluded that STEM with an annular detector such as the HAADF has the advantage of sequential scans using a beam of highly focused electrons over a selected area. The detectors are designed to acquire electrons from various scattering angles other than the original propagating beam. This technique allows the user to acquire images by collecting electrons that had undergone various types of diffraction and scattering processes and provide highly vital physical

information when the electrons interact with the sample. Additionally, the ability to reconstruct a 3-D morphology from an HAADF-HRSTEM image is a major advantage of this characterization method.

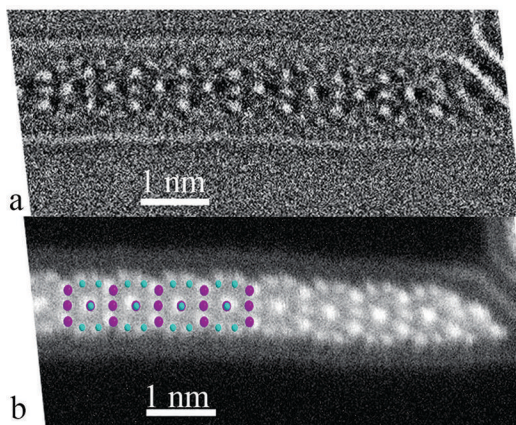


Figure 2. 1-D CuI inside an SWCNT as seen in an HRSTEM image in (a) bright field mode and (b) dark field mode with a simulated model of the CuI unit cell. Adapted with permission from ref. (23). Copyright 2016 Wiley.

Scanning Tunneling Microscopy

The STM technique is used to image the supported individual metal atoms (27, 28). STM generally runs at low temperature under ultrahigh vacuum to enhance the resolution of STM to examine single atoms (29, 30). Lucci et al. (31) used STM to identify a single Pt atom deposited on Cu(111) surfaces. The result obtained by STM imaging showed that at low Pt coverage (0.02 monolayer), the Pt atoms exist as individual and isolated species substituted in the Cu surface lattice, so this is referred to as a “single-atom alloy” (SAA) (32). The Pt atoms were added into Cu(111) terraces and in the areas above the surface edges by place exchange (Figure 3a,b). STM imaging can allow visualization of the atomic-scale structure of surfaces around single atoms during reactions. It helps in the examination of reaction mechanisms and single-atom sintering (33). Lucci et al. (31) studied the ability of Pd monomers (Pd coverage ≤ 0.05 monolayer) to exist as isolated atoms substituted into the Au lattice (34–36). At Pd coverage greater than 0.05 monolayer, Pd atoms start to form clusters due to kinetic limitations (37) on a Au(111) surface for H₂ activation (38). Here STM was utilized to visualize the atomic composition of the active sites directly. The result clearly is shown, with the help of coupling high-resolution STM and temperature-programmed desorption, that at low concentration the individual and isolated Pd atoms dissociate H₂, as the absorbed concentration of H atoms was proportional to the surface Pd atoms in Au. Liu et al. (39) using STM investigated the atomic-scale interactions of CO and H with Pt catalytic sites on Pt-Cu(111) SAA surfaces (Figure 3c–e) and suggested that the selective adsorption of CO took place on Pt sites and that H atoms were capable of diffusing into Cu sites.

STM is a surface-science technique. STM analysis can have a lateral resolution of 0.1 nm and depth resolution of 0.01 nm (10 pm) (25). STM can do characterization of catalysts with a uniform, flat structure. It can investigate both geometric and electronic structures and helps in the identification of elements with close atomic numbers (40). For example, N-doped carbon materials, which are one of the typical metal-free catalysts, to make N atoms visible in them, are important

for the identification of active sites. Deng et al. (41) used low-temperature STM to examine the N-doped graphene at the atomic scale. The area brighter than the main 2-D graphene network (Figure 4a) indicated the presence of defects and that the electronic structure of N-doped graphene was disturbed by N-dopants. The sizes of the bright areas were smaller than 0.5 nm. DFT calculations were performed to gain further insight into the doping effect on the structure of graphene. So via STM simulations (Figure 4b), the bright spots were found to be C atoms adjacent to N, and the C atoms exhibited higher brightness because of the increased electron density of states near the Fermi level (42). Zhao et al. (43) also reported a low-temperature STM investigation of N-doped graphene derived by chemical vapor deposition. It showed a local structure of one N atom as a bright triangular spot confined in the graphene lattice (Figure 4c), confirmed by their STM simulations (Figure 4d). STM has proven to be an important spectroscopy technique to explore the surface science and imaging surfaces at the atomic level. Through this technique, individual atoms within materials can be imaged, visualizing the atomic composition of the active site, manipulated by changing the working conditions, such as ultrahigh vacuum, air, water, and various other liquids and gases (44).

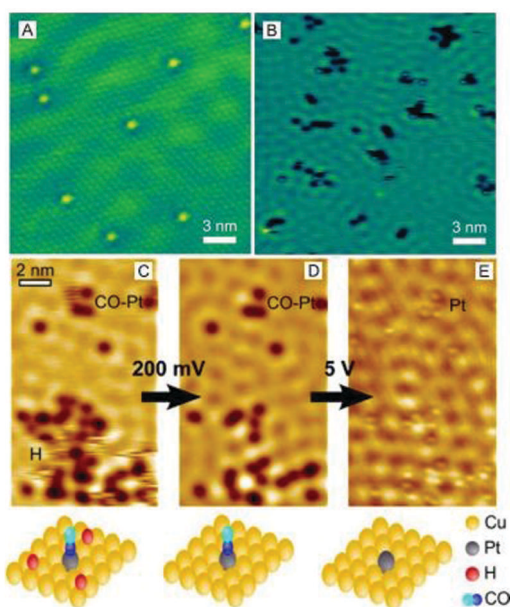


Figure 3. (A) STM image of Pt/Cu(111) SAA surface in which Pt atoms appear as isolated protrusions substituted into Cu. (B) STM image showing H atom spillover onto Cu; H appears as clusters. Pt appears as protrusions, and (C–E) STM shows adsorption of H and CO on Pt-Cu(111) SAA surface. (A,B) Adapted with permission from ref. (31). Copyright 2015 Nature Publishing Group. (C–E) Adapted with permission from ref. (39). Copyright 2016 American Chemical Society.

Scanning Electron Microscopy with Energy-Dispersive X-ray Spectroscopy

Scanning electron microscopy along with energy-dispersive X-ray spectrometry (SEM-EDX) helps in investigating the morphology and dispersion of nanoparticles (NPs) on a surface, accurately measuring the lateral dimensions of NPs, and studying their elemental composition (45). SEM helps in the analysis of the morphology and topography and provides information about the crystallographic nature of the analyzed specimens (46). Tang et al. (47) investigated the use of a Pd/CeO₂ nanocatalyst for the development and optimization of a novel solid-phase activation

method for lignite-derived humic acid. The morphology and elemental composition of the NPs were analyzed by SEM-EDX. The SEM-EDX of CeO₂ and Pd/CeO₂ are shown in Figure 5i.a–d. The EDX spectra from the synthesized CeO₂ show Ce and O, indicating the high purity of the as-synthesized samples. After the addition of Pd, then Pd, O, and Ce were observed (Figure 5i.b,d). The EDX spectra confirmed that the Pd NPs were highly dispersed on the surface of the CeO₂ support, which corresponded with the result obtained from the HR-TEM image. Han et al. (48) synthesized MgF₂ fibers and subnano MgF₂ embedded in carbon nanofibers by one-step electrospinning. For the morphology investigation, an SEM at an accelerating voltage of 15 kV equipped with EDX was used. The elemental mapping analysis revealed the composition of the fibers, namely C, F, and Mg. Trace amounts of impurity, oxygen, and copper were detected. The atomic contents of C, O, F, and Mg were determined to be 78.6%, 1.5%, 12.2%, and 7.8%, respectively. From the mapping analysis, it is noticeable that MgF₂ is uniformly distributed in the carbon structure. SEM images show that the fibers obtained are straight, smooth, and clear (Figure 5ii.a,b,d,e,g,h). The average diameter of the fibers was 171 nm (Figure 5ii.c), which decreases to 148 nm after calcinating at 650 °C in N₂ (Figure 5ii.f), keeping the morphology almost unchanged. The structure of the fiber is also preserved on calcination in air at 650 °C (Figure 5ii.g,h). Lastly, MgF₂ is fabricated with a decrease in diameter from 171 nm to 106 nm (Figure 5ii.i).

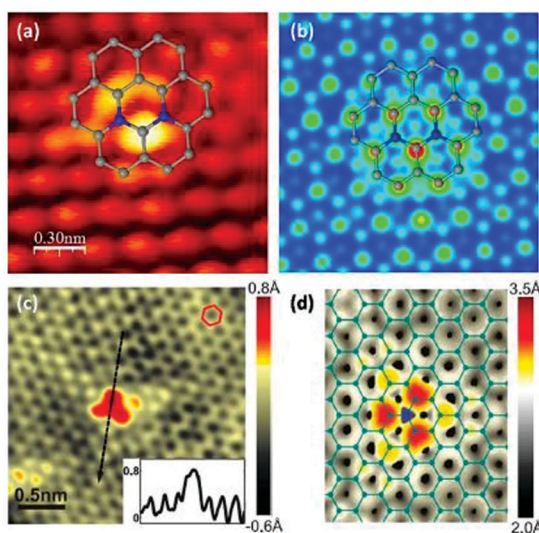


Figure 4. (a) STM image of N-doped graphene. (b) Simulated image of (a). (c) STM image of N-doped graphene (derived by chemical vapor deposition). (d) Simulated image of (c). (a, b) Adapted with permission from ref. (41). Copyright 2011 American Chemical Society. (c, d) Adapted with permission from ref. (43). Copyright 2011 American Association for the Advancement of Science.

Klaysri et al. (49) studied the synthesis of N-doped and Si-doped TiO₂ nanocatalyst powdered and grafted onto a poly(methyl methacrylate) film. SEM-EDX was used to investigate the morphology and the elemental composition of particles grafted onto the film. The SEM image showed that the grafting process successfully grafted the TiO₂ particle onto the film. The EDX estimated the bulk composition on the poly(methyl methacrylate) film, and the SEM images corresponded with the EDX result. Pascariu et al. (50) prepared Ni/Co codoped ZnO NPs via the coprecipitation method. SEM-EDX was used to analyze their structural and morphological

properties. SEM was carried out in a high vacuum at a suitable acceleration voltage, and the elemental mapping was collected at magnification $\times 10,000$ with a large acquisition time (more than 80,000 counts). In the SEM images, it was observed that the doped ZnO nanoparticles are rod-like, and the concentration of dopants moderately influenced their size, morphology, and aggregation degree (Figure 6a–d). A lower concentration of dopants leads to smaller nanorods, and as the concentration increases, the nanorods become more homogeneous in shape and size and agglomerate less. EDX was used for a composition characterization of Ni/Co codoped ZnO nanoparticles, and the chemical mapping showed the doping homogeneity of Zn, O, Ni, and Co. Blass et al. (51) synthesized lanthanide (Ln = La, Eu, Gd, Dy, and Ho) loaded ZnO catalysts (Ln-ZnO) and characterized them. SEM-EDX micrographs and elemental mapping analysis were used to investigate the morphologies of 0.25 M ZnO and 1% Ln-ZnO catalyst. In 0.25 M ZnO, the NPs were spherical, and EDX analysis detected Zn and O. However, the addition of Ln ions changed the structure. It was observed that the NPs accumulated in certain regions with smaller grain sizes, which were interpreted as available adsorption sites. The EDX analysis showed La, Eu, Gd, Dy, and Ho in addition to Zn and O. The combination of SEM imaging and elemental analysis by EDS spectroscopy has been widely used for the characterization of nanocatalysts.

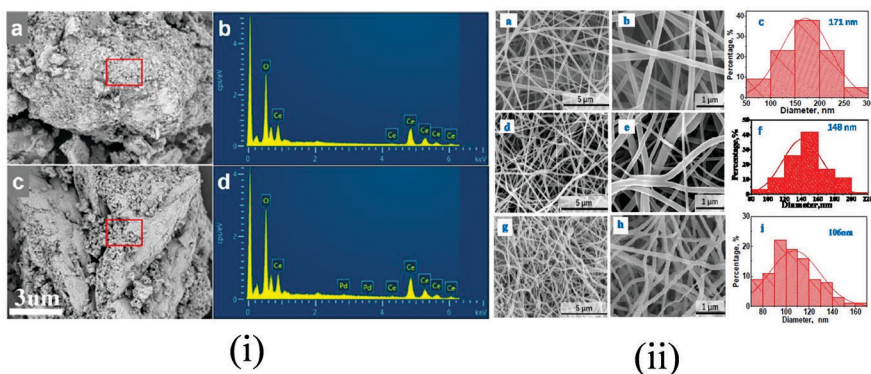


Figure 5. (i) SEM-EDX of CeO_2 and Pd/CeO_2 catalyst: (a) SEM image CeO_2 catalyst. (b) EDX spectrum of square portion of (a). (c) SEM image of Pd/CeO_2 catalyst. (d) EDX spectrum of square portion of (c). Reproduced with permission from ref. (47). Copyright 2017 American Chemical Society. (ii) SEM images of nanofibers (a, b, d, e, g, h), and diameter distributions of fibers (c, f, i). Reproduced with permission from ref. (48). Copyright 2017 Royal Society of Chemistry.

Energy Dispersive X-ray Spectroscopy

Energy dispersive X-ray spectroscopy plays a vital role in the qualitative and quantitative elemental analysis of NPs, and it helps in determining their composition and confirming the stoichiometry (52, 53). Characteristics of the elements are represented by the X-rays emitted from the atoms, and their intensity distribution represents the thickness-projected atom densities in the specimen (54). Nadjia et al. (53) synthesized CeO_2 NPs in an alkaline medium by using the homogeneous precipitation method and later calcinated the same at 80°C for 24 h (CeO_2 -80) and 500°C for 2 h (CeO_2 -500). Here the EDX technique was used to confirm the stoichiometry of CeO_2 NPs, carried out at 20 kV. The EDX technique was used to investigate the atomic concentration of Ce and O on the top layer surface of CeO_2 -500 (Figure 7a). The atomic abundances of Ce and O present on the uppermost surface and in the bulk layers of CeO_2 -500 were compared, and the data

revealed that the surface O/Ce ratio (2.13) was close to the bulk O/Ce ratio (2.00), suggesting that the samples have an intrinsic effect that would affect their photocatalytic activity.

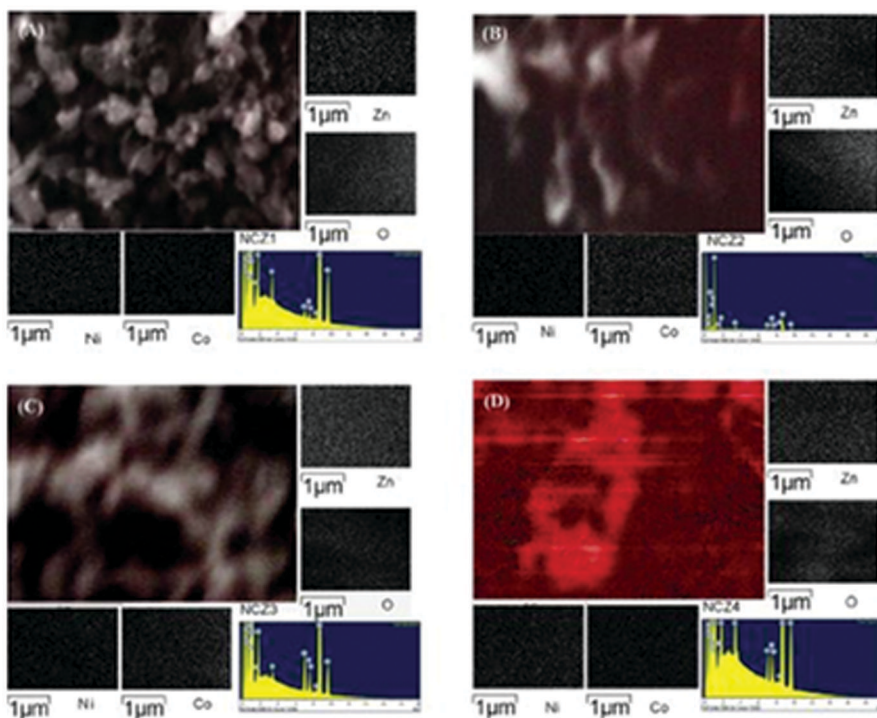


Figure 6. SEM-EDX characterization, elemental mapping, and spectrum of Ni/Co doped ZnO nanoparticles with different concentrations of dopant. Reproduced with permission from ref. (50). Copyright 2019 Elsevier.

Mahajan et al. (55) prepared Pd NPs with a varying diameter (6.9–25.1 nm) in the presence of poly(vinyl alcohol) by a single-pot wet chemical technique, followed by adsorption on Ni foil. The investigation of the morphology and surface characteristics of the Pd nanocatalyst was done by electron microscopy in conjunction with energy dispersion spectroscopy. The EDX study analyzed the surface composition of each electrode. As shown in Figure 7b, the atomic ratio of C:O for all electrodes was around 2:1, indicating the coexistence of poly(vinyl alcohol) with NPs of metal adsorbed on the surface of Ni. From the data computed based on the EDX data (Figure 7c), it was revealed that with an increase in particle diameter, the moles of Pd adsorbed per unit area increases initially, and it decreases quickly when the average diameter reaches 21.3 nm because of less interaction with poly(vinyl alcohol) and the Ni surface.

Ganeev et al. (56) presented the results of systematic studies of the nonlinear optical properties of BaTiO₃ and SrTiO₃ nanoparticles and studied their structural characteristics. By using EDX spectroscopy, they did the elemental analysis of the NPs and confirmed the presence of BaTiO₃ and SrTiO₃. Rahman et al. (57) synthesized a magnetically separable spinel CuFe₂O₄ nanocatalyst by the coprecipitation method and characterized it. The EDX spectra of the spinel CuFe₂O₄ nanoparticle confirmed the presence of copper, iron, and oxygen with an oxygen:copper ratio of approximately 2:1 (Figure 8a). Similarly, Khazaei et al. (58) reported a green, solvent-free synthesis of polyhydroquinoline using a nano-CoAl₂O₄ catalyst. Here also EDX was used for elemental analysis

of nano-CoAl₂O₄, and the spectrum indicated the existence of cobalt, aluminum, and oxygen (Figure 8b). Valan et al. (59) synthesized spinel Mn_xCo_{1-x}Al₂O₄ ($x = 0, 0.3, 0.5$) nanoparticles using the *Sesamum indicum* plant extracted by the microwave-assisted combustion method. EDX was used for the elemental composition analysis; the spectra showed the peaks of Mn, Co, Al, and O in the spinels CoAl₂O₄ and Mn_{0.5}Co_{0.5}Al₂O₄, and there is no other peak, confirming that the synthesized NPs are pure. In the spectrum of both samples, a small peak appeared at 2.1 kV, indicating the presence of Au (gold), which appeared because gold was used as a sputter coating while preparing the samples for high-resolution SEM imaging. Mainly EDX is used for elemental analysis of nanocatalysts.

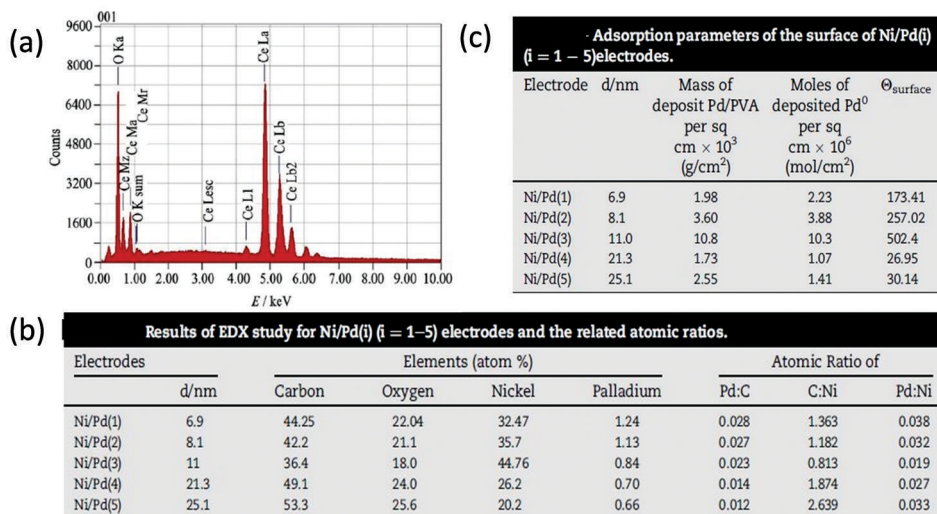


Figure 7. (a) EDX spectrum of CeO₂-500 nanocatalyst. Reproduced with permission from ref. (53). Copyright 2018 Elsevier. (b) Table showing element atomic ratios of C:O. (c) Table showing the computed data based on EDX data. (b, c) Reproduced with permission from ref. (55). Copyright 2017 Elsevier.

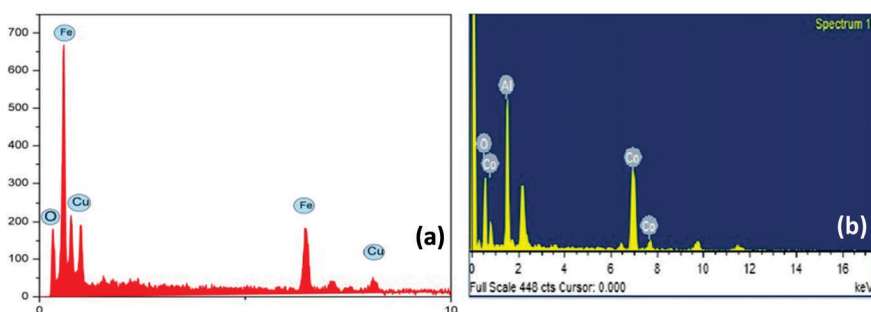


Figure 8. (a) SEM-EDX of CuFe₂O₄. Reproduced with permission from ref. (57). Copyright 2020 Springer. (b) EDX spectrum of the nano-CoAl₂O₄. Reproduced with permission from ref. (58). Copyright 2017 Wiley.

Tip-Enhanced Raman Spectroscopy

Tip-enhanced Raman spectroscopy (TERS) is an optical imaging tool that can characterize nanomaterials through a plasmonic-nanocavity-generated confined electromagnetic field with interaction length on the order of subnanometers (60). This method can provide chemical sensitivity

and an impressive spatial subnanometer resolution when used in combination with STM images (61). The combined advantages of Raman spectroscopy and scanning probe microscopy make TERS a powerful tool for analysis, providing high sensitivity and resolution for local investigation and imaging of materials such as 2-D monolayers, as shown in Figure 9 (62). Additionally, important chemical information can also be inferred because low-temperature TERS has a high spatial resolution with single-molecule sensitivity.

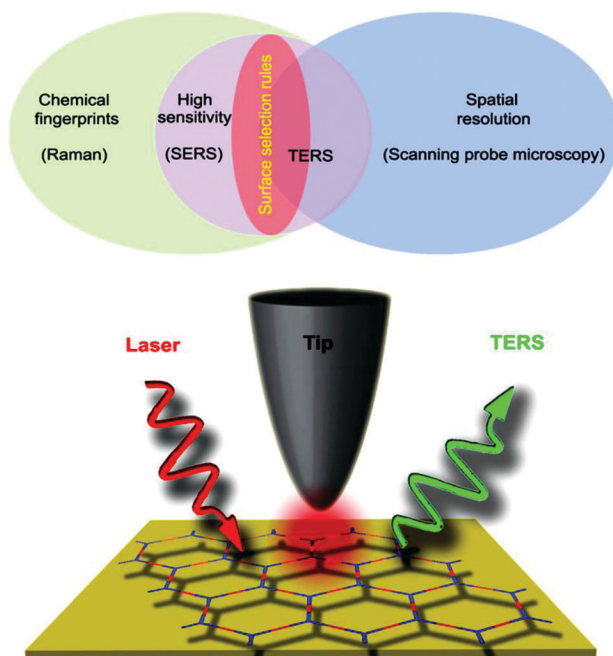


Figure 9. Benefits of TERS in a Venn diagram and scheme representing the TERS for imaging monolayers. Reproduced with permission from ref. (62). Copyright 2019 Springer.

Liu et al. (63) used tip-enhanced resonance Raman spectroscopy along with scanning tunneling spectroscopy to study epitaxially grown ZnO layers on a Ag(111) surface. Balois et al. (64) used a combination of TERS-based imaging and analysis to establish strain variations in defect-free monolayer graphene on a Au(111) substrate. As shown in Figure 10, TERS-based Raman spectra were recorded for graphene and bare Au(111). Three peaks (D, G, and 2D) are observed in Figure 10b from the TERS imaging observed upon averaging in three different domains. The authors report the disappearance of these peaks when the tip is far-field or retracted and thus can confirm the enhanced Raman signals. Additionally, intensity, Raman shift, and spectral width were also measured for all of the bands observed, which is essential as any change in chemical and mechanical interactions can be observed in the spectral lines (65). The line scan in Figure 10c shows 0.7 nm spatial resolution (64).

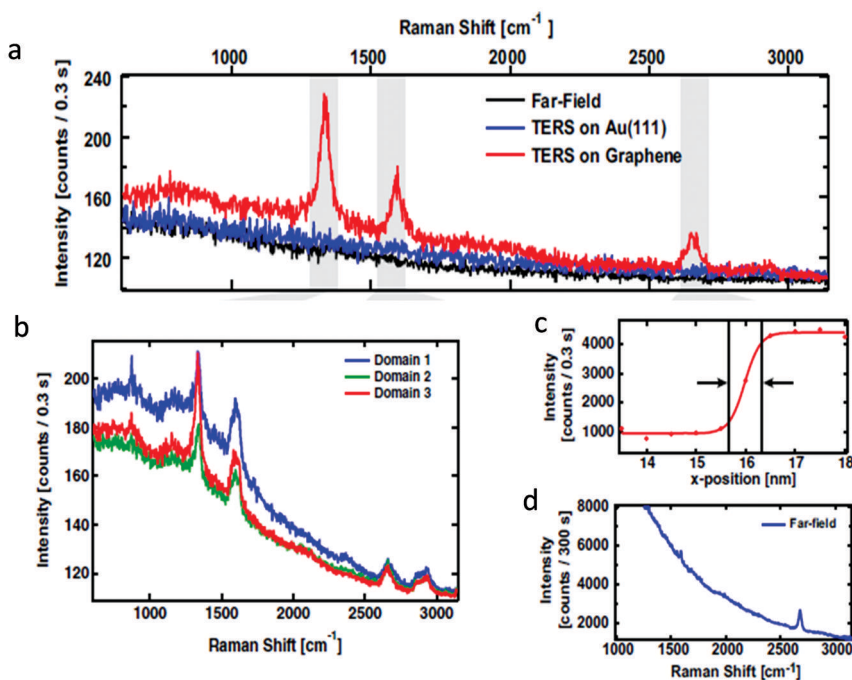


Figure 10. (a) TERS on graphene (red), Au(111) substrate, and far-field Raman (tip retracted); (b) average TERS; (c) line profile of step response; and (d) long-exposure measurement of far-field Raman. Reproduced with permission from ref. (64). Copyright 2019 Nature Publishing Group.

Ichimura et al. (65) performed a one-dimensional scan of SWCNTs to probe the extent of spatial resolution using TERS. Additionally, they also studied the mechanical and chemical interactions in nanocrystal adenine with a precise tip-sample distance. Figure 11 represents a schematic that Ichimura et al. used for analyzing with high precision by illuminating for a chosen tip-sample distance. The tip oscillates sinusoidally, synchronizing with the opening of the time gate, as illustrated in Figure 11b (66). The temporal width (Δ) and the time delay (τ) of the time gate are selected in accordance with the desired tip-sample distance. This is accomplished by feeding a trigger signal to the pulse generator extracted from the tip oscillation. This results in the synchronous generation of a pulse signal that controls an optical shutter via a modulator, which in turn performs the illumination depending on the tip-sample distance. Zhang et al. (67) used a high-quality and clean tip and sample under ultrahigh vacuum and low temperature for excellent reproducibility. They showed that the tip, when positioned on the bare surface, gives a featureless continuum spectrum, indicating that no molecules are present and the tip is free of contamination. However, on top of island molecules, vibrational fingerprints of molecules were visible in the TERS spectrum. These vibrational fingerprints are provided via STM-controlled TERS while employing an excitation field, which can be observed in the spectrum even under low bias voltage, and thus it can be inferred that the localized tunneling of electrons does not affect the TERS spectrum signals (67, 68).

Consequently, numerous factors contribute to achieving a subnanometer resolution in TERS, such as nanofeatures on the substrate, step size of the mapping, thermal diffusion of the molecule, incident laser angle, and polarization. Additionally, an ultrahigh vacuum and low-temperature setup help to provide resolution down to subnanometers (69). Thus, it can be concluded that TERS is a powerful and versatile technique that incorporates and combines the advantageous features of various other techniques including SERS, Raman, and scanning probe microscopy. This

amalgamation makes TERS a tool that is highly selective and sensitive with a high spatial resolution for characterization.

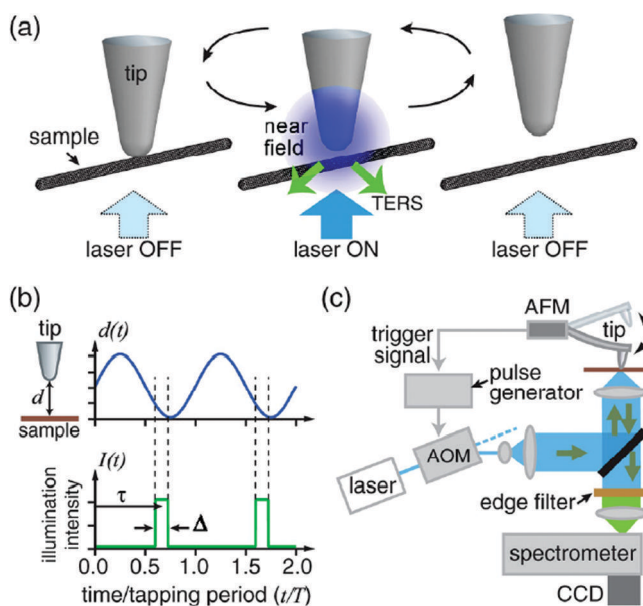


Figure 11. (a) Tip–sample arrangement illuminated for predecided distance. (b) Illustration representing sinusoidal oscillation of the tip and synchronized opening of the time gate. (c) TERS using tapping mode and acoustic–opt modulator for time-gated illumination. Reproduced with permission from ref. (65). Copyright 2009 American Physical Society.

X-ray Reflectometry

X-ray reflectometry is a form of nondestructive characterization where X-rays are directed at varying angles and a photodiode detects the reflected radiation. X-ray reflectometry is a general tool for characterization of multilayers with angle-resolved XRF and can be suitably used to characterize multilayers with subnanometer thickness (70). Subnanomaterials used in multilayer interferential mirrors hold special importance as they are used for applications relating to plasma diagnostics, extreme ultraviolet (EUV) photolithography, and solar corona imaging, which uses the X-ray and EUV spectrum. In order to smooth interfaces and limit the interdiffusion, subnanometer-thick barrier layers are used in the EUV spectral region. Applications include hard X-ray telescopes (71), normal incidence broadband coatings (72), and grazing incidence mirrors (73). The grazing incidence X-ray reflectometer (GIXRF) shown in Figure 12 uses a shallow incidence angle for the primary X-ray radiation and can be used to define the thickness of subnanometer materials in a periodic structure. There is an enhancement of excitation due to X-ray standing wave formation, for which the essential requirement is the use of a low-divergence monochromatic primary beam generated by an X-ray tube or a synchrotron facility (74, 75).

The incident and reflected X-ray beams interfere at the layer boundaries, leading to the formation of constructive and destructive nodes (76). GIXRF measures below the total angle of reflection and then surpasses it (77). In this technique, the sample is tilted at a defined angle with respect to the beam, with the detector placed above it. The detector, usually a silicon drift detector, is energy-dispersive. Emprin et al. (78) used a “Fabry–Perot” type structure to determine the thickness of

subnanometers embedded between similar periodic multilayers. They used periodic chromium/scandium layers with a Sc layer between with highly precise control for the study.

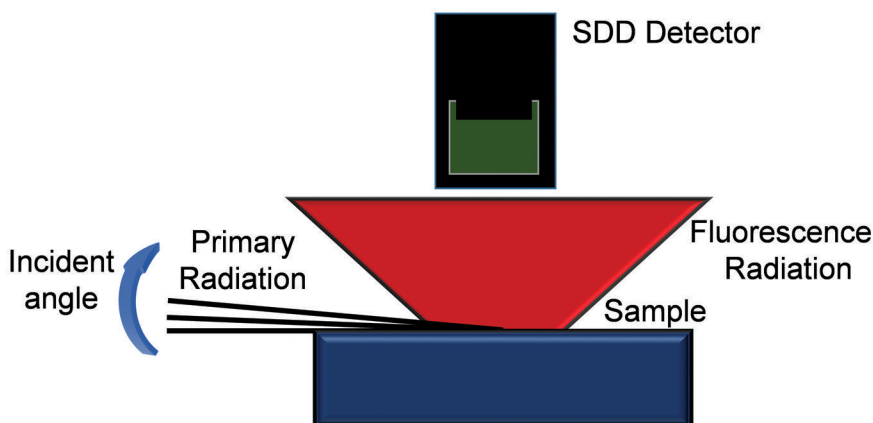


Figure 12. Schematic diagram showing the geometry of GIXRF.

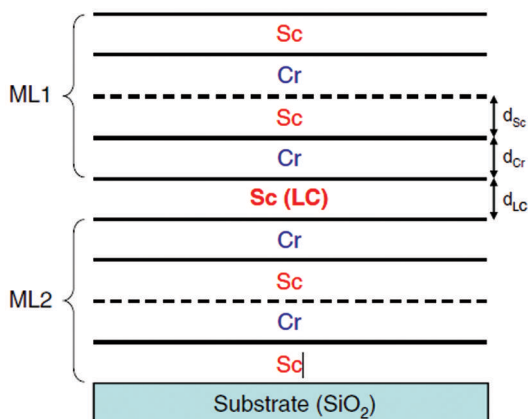


Figure 13. Fabry-Perot type multilayer with Sc calibration layer positioned between two periodic multilayers ML1 and ML2. Reproduced with permission from ref. (78). Copyright 2014 Elsevier.

The Fabry-Perot structure is as given in Figure 13, with the calibrating layer (LC), which is Sc, between multilayers ML1 and ML2. The acquisition and extinction of the Bragg peak is highly sensitive and dependent on the thickness of the layers, that is, d_{LC} and d_{SC} , and are synchronous to the phase of the waves reflected from ML2 and ML1. Haase et al. (79) used various characterization techniques such as EUV and X-ray reflectance to study Cr/Sc multilayer systems, which are useful as near-incidence mirrors. They were able to deduce that the individual layer was less than 1 nm. The GIXRF analysis uses fluorescence data with photons having an excitation energy of 6.25 keV. Using GIXRF, they successfully resolved the interdiffusion layer thickness, the Sc/Cr ratio, and the spatial arrangement of the multilayer structure.

X-ray Absorption Spectroscopy

X-ray absorption spectroscopic (XAS) analysis enables the element-specific atomic site analysis of the local structure and electronic characterization of metal nanoclusters. The XAS involves

electronic transitions from core levels to the unoccupied valence states from the X-ray absorption process.

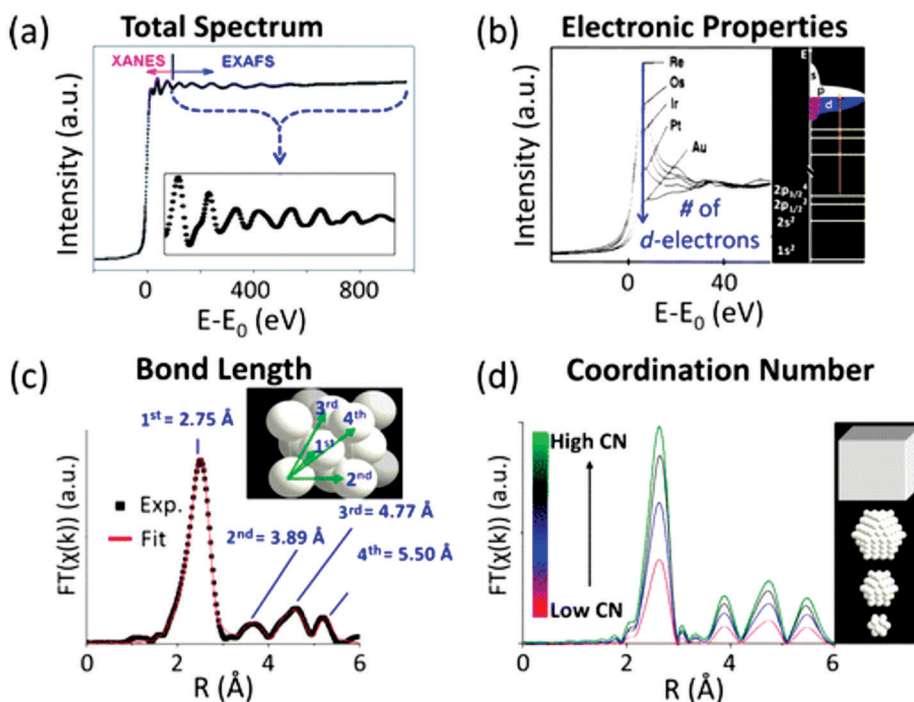


Figure 14. (a) XAS spectrum consisting of both EXAFS and XANES with k -space EXAFS spectrum on the inset. (b) L_3 -edge XANES spectra of a few 5d transition metals. (c) EXAFS spectrum with the best fit of Pd foil along with structure model. (d) Illustration demonstrating the simulated EXAFS with increasing coordination number. Reproduced with permission from ref. (80). Copyright 1992 American Chemical Society.

A typical XAS spectrum is determined by two spectral regions: X-ray absorption near-edge structure (XANES) and extended X-ray absorption fine structure (EXAFS; Figure 14a). XANES provides the element-specific analysis by probing the electronic properties of absorbing atoms in the near-edge region. For instance, the intensity of the first spectral feature (Figure 14b) is sensitive to the unoccupied valence d state. By monitoring the intensity, holes in the d state can be ascertained. Accurate information on the local structure of absorbing atoms, for example, bond length and coordination number (Figure 14c,d), can be acquired by EXAFS (81).

MacDonald et al. (82) conducted the first XAS study on truly monodispersed thiolate-protected Au_{144} nanoclusters (Au SR NCs). The structural information acquired by an EXAFS fitting analysis (Figure 15b) was consistent with the structural model determined by DFT given by Lopez and Acevedo (Figure 15a). A comparative study illustrating the electronic and bonding properties of Au_{144} , Au_{38} , and Au_{25} was done using Au L_3 -edge (Figure 15d) and S K-edge (Figure 15e) XANES (80).

Later, MacDonald and coworkers (83, 84) also reported an EXAFS study for Au_{38} SR NCs (structural model shown in Figure 16a) in solid and toluene solution (Figure 16b). The solvation

process of Au₃₈ NCs resulted in the expansion of Au–Au bonds, sensitively probed by an EXAFS fitting analysis (80).

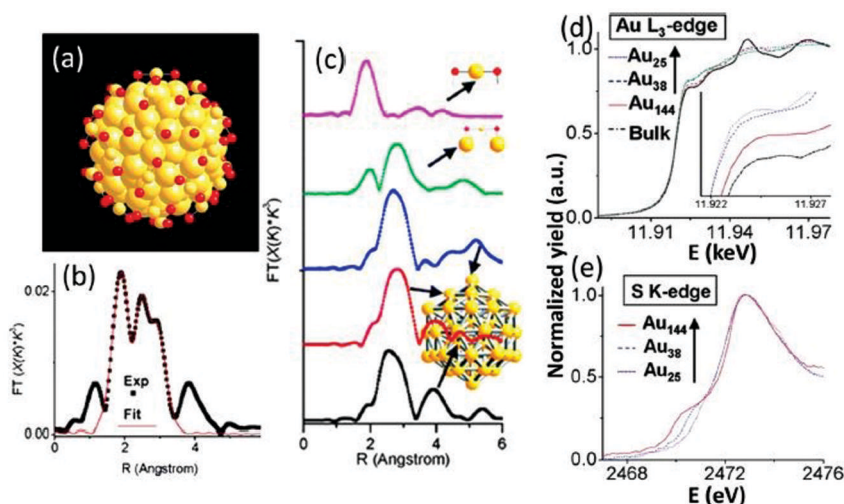


Figure 15. (a) DFT-predicted structural model and (b) experimental and best-fit EXAFS of Au₁₄₄. (c) DFT structural model simulated site-specific EXAFS. (d) Au L₃-edge and (e) S K-edge XANES of Au₁₄₄. Reproduced with permission from ref. (82). Copyright 2010 American Chemical Society.

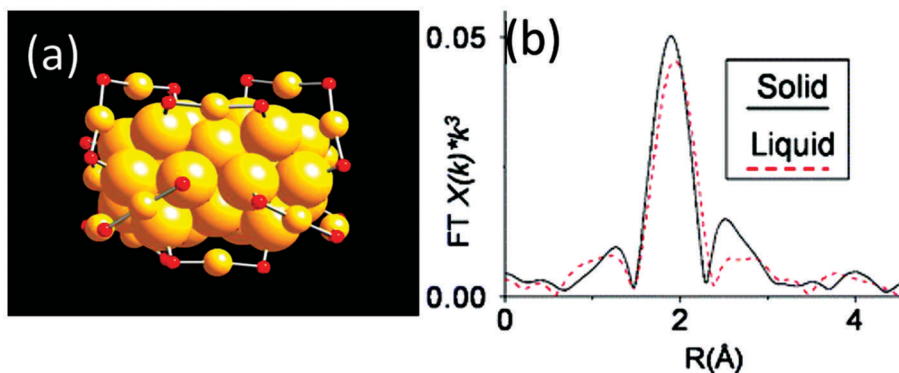


Figure 16. Structural model (a) and EXAFS (b) of Au₃₈ in solid and solution phases. Adapted with permission from ref. (83). Copyright 2011 American Chemical Society.

They also conducted a multishell EXAFS fitting strategy on Au₂₅ SR NCs (Figure 17a) to monitor their structural change in different temperatures and solvent conditions. The site-specific simulation spectrum (Figure 17b) showed distinct EXAFS peaks corresponding to unique scattering paths, including Au–S and three Au–Au paths. EXAFS fitting results of the Au–thiolate cluster (Au SR NCs) in solution phase samples (toluene and acetonitrile as solvents) and solid phase at different temperatures (10 vs. 300 K) are compared in Figure 17c. It shows a general decrease in the bond length of the Au₁₃ core [i.e., (Au–Au)₁ and (Au–Au)₂] with an accompanying increase in the Au(kernel)–Au(staple) [(Au–Au)₃] bond length when solvated in toluene. When the Au SR NCs were solvated in polar solvent acetonitrile, further shrinkage of the Au₁₃ core was noticed, with no effect on (Au–Au)₃ relative to that of the solid phase. Overall, the structural changes in Au₂₅ NCs

illustrated the interplay of the “metallic” behavior of the Au₁₃ core and the “molecular” behavior of the gold–thiolate ligand shell.

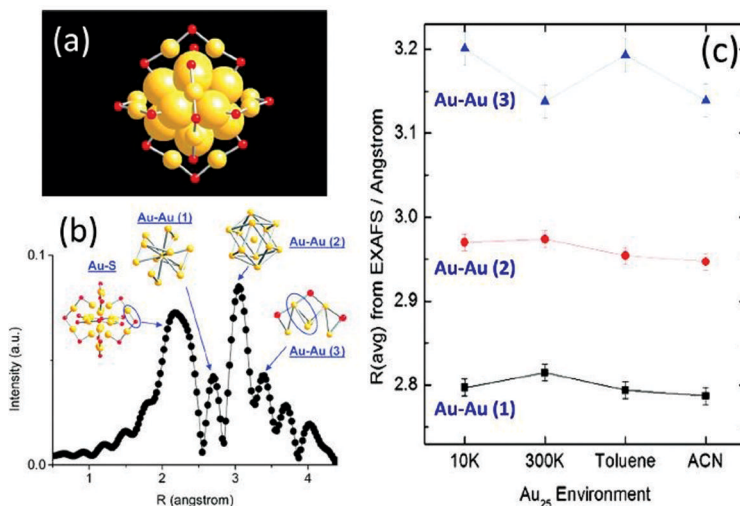


Figure 17. Structural model (a) and simulated EXAFS (b) of Au₂₅. (c) Bond distance fitting obtained from EXAFS of Au₂₅ under various environments. Adapted with permission from ref. (84). Copyright 2011 American Chemical Society.

Christensen et al. (85) used XAS to probe structure and bonding and Pt position in a thiolate-protected PtAu₂₄(SR)₁₈ nanocluster. The three possible locations of Pt dopant corresponded to different Pt–Au coordination number shown in Figure 18B–D. Au L₃-edge EXAFS showed a narrowing line-shaped Au 4f peak of PtAu₂₄ due to metal–metal bond contraction resulting from the Pt doping effect. It was also observed that the Au 4f peak shifted to lower binding energy, which could be related to the Pt–Au alloy bonding effect, as shown in Figure 18F.

The XAS study by Chevrier and coworkers (86, 87) compared the structural and electronic property sensitivity with a small change in core size (C₁₃ vs. C₁₉) in gold–thiolate nanoclusters, Au₁₉(SR)₁₃ and Au₂₅(SR)₁₈, respectively (the structural model is shown in Figure 19a). Au₁₉(SR)₁₃ showed a different valence electron behavior with a narrowed and positively shifted band, illustrating the more metallic nature relative to Au₂₅(SR)₁₈, as shown in Figure 19b. Further, a multishell EXAFS fit (Figure 19c) was conducted for a detailed correlation of electronic properties with atomic structure. The results revealed a considerable Au–Au bond expansion of surface–surface and the surface-stable Au atoms. In contrast, the bond distance between Au–S and center-surface (Au–Au) remains unchanged.

Zhang et al. (88) demonstrated that encapsulation within carbon nanotubes facilitates the oxidation activity of Pt NCs. In situ XANES revealed that encapsulation restricted the Pt NC size to 1 nm and rewardingly enabled the retention of Pt species at an active reduced state, protected from oxygen up to 200 °C. The XANES spectrum of Pt/CNT and the reduced Pt@CNT catalyst exhibited features similar to that of Pt foil. The radial structural function comparison curves derived from the EXAFS function’s Fourier transform also suggested the Pt–Pt interaction and absence of Pt–O interaction. This confirmed the prior reduction of Pt clusters in both Pt@CNT and Pt/CNT. The Pt L_{III}-edge of Pt/CNT and the situ radial structural function revealed the appearance of the

Pt–O scattering paths during toluene oxidation, which become more prominent on increasing the temperature.

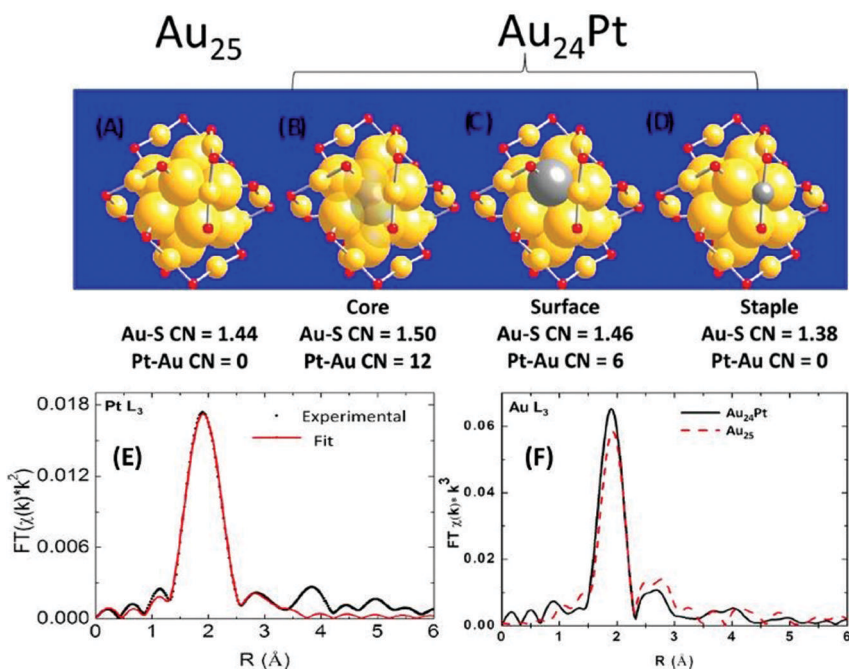


Figure 18. (A)–(D) Representations of structural models and CN values of Au₂₅ and Au₂₄Pt with varying dopant location. (E) Pt L₃-edge EXAFS and its best fit of Au₂₄Pt. (F) Au L₃-edge EXAFS of Au₂₅ and Au₂₄Pt. Reproduced with permission from ref. (85). Copyright 2012 American Chemical Society.

Meanwhile, the white-line intensity was enhanced, which reflected the 5d states' unoccupancy and indicated the oxidation state variation. This confirmed the oxidation of Pt species over the CNT exterior walls. In contrast, the Pt–O scattering was not observed for Pt@CNTs even in oxygen up to 200 °C with no variation of the white-line intensity.

Yamazoe et al. (89) used Au L₃-edge EXAFS spectroscopy and corresponding FT-EXAFS spectra to investigate the bond stiffness and hierarchy in thiolate-protected gold clusters (Au SR NCs), namely Au₂₅(SR)₁₈, Au₃₈(SR)₂₄, and Au₁₄₄(SR)₆₀. The long Au–Au bonds of the icosahedron-based Au core surface were found to be flexible relative to the bulk metal, whereas the short Au–Au bonds distributed in the radial direction of the Au core were stiffer than those in the bulk metal and formed a ring structural backbone with the rigid Au–SR oligomeric framework that enhances Au–Sr NC thermal stability. The temperature dependence of the Debye–Waller factors of the individual bonds was analyzed within the Einstein model framework. It showed that the Einstein temperatures of the Au–Au(S) and Au–Au(L) bonds and that of Au–Au bonds in bulk Au were a function of cluster size. This plot indicated that Au–Au(S) and Au–Au(L) bonds were respectively stiffer and more flexible than the cubic bulk Au–Au bonds. The correlation suggested that the bond stiffness and bond length are correlated. This hypothesis was confirmed by plotting Einstein temperatures of Au–Au bonds as a function of their lengths.

XAS analysis is used to probe materials and determines quantitative information for the local physical structure, shape, and electronic properties in supported metal nanostructures and bimetallic nanosystems. XAS spectroscopy provides insight into changes that occur in the local bonding

environment by measuring accurately the bond distance. This helps in tailoring the structural properties of the metal nanoclusters with a change in the chemical environment.

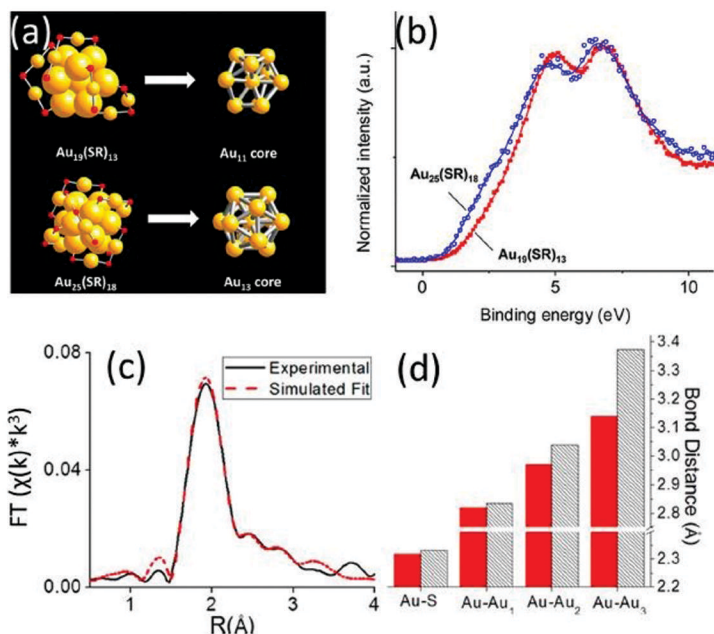


Figure 19. (a) Illustration representing structural models. (b) XPS valence band data of Au_{19} and Au_{25} . (c) EXAFS and best fit. (d) Graph showing comparison of bond distance from the EXAFS fitting results of Au_{19} (stripes) and Au_{25} (red). Reproduced with permission from ref. (86). Copyright 2012 American Chemical Society.

Infrared and Associated Spectroscopy Techniques

Direct monitoring of the probe/adsorbed molecules interacting with the surface of supports such as metal catalysts is vital in the characterization of the metal catalyst (90). Infrared spectroscopy and its subsidiaries, in combination with investigative techniques, are powerful tools that provide a description of catalyst surface properties by monitoring the probe–surface interaction (91). This is an indirect method whereby the study of the surface is observed through the perturbation in the probe. The change in intensity of the probe and the vibrational frequency are monitored to infer the properties of the active centers (92).

Techniques such as time- and temperature-resolved Fourier transform infrared spectroscopy can be used to monitor and study intermediate species formed in the reaction (93). The oxidation state and dispersion state of single-atom catalysts (SACs) are generally monitored by a gas like CO, whereby the initial state frequencies of CO change when it is bound to the SAC (94). As the vibration modes are highly sensitive to the adsorbed CO species, it effectively traces the reaction pathways on reactions catalyzed by CO. It imperviously proves the presence of single-site catalysts, eliminating the presence of nanoparticles (95). Thus, the IR technique can be successfully implemented for probing the electronic and structural states of the catalyst where CO adsorption on different metals leads to different vibration bands, which in turn affect the adsorption models and the electronic states in the IR spectra (96). For example, Yan et al. (96) found different adsorption bands depending on the adsorption model. Linear and bridge are observed; for example, ionic Pt, metallic Pt, and Pt clusters

indicated different bands based on the absorption spectra. Thus, SACs having high dispersion indicated a strong signal for adsorption by ionic metals.

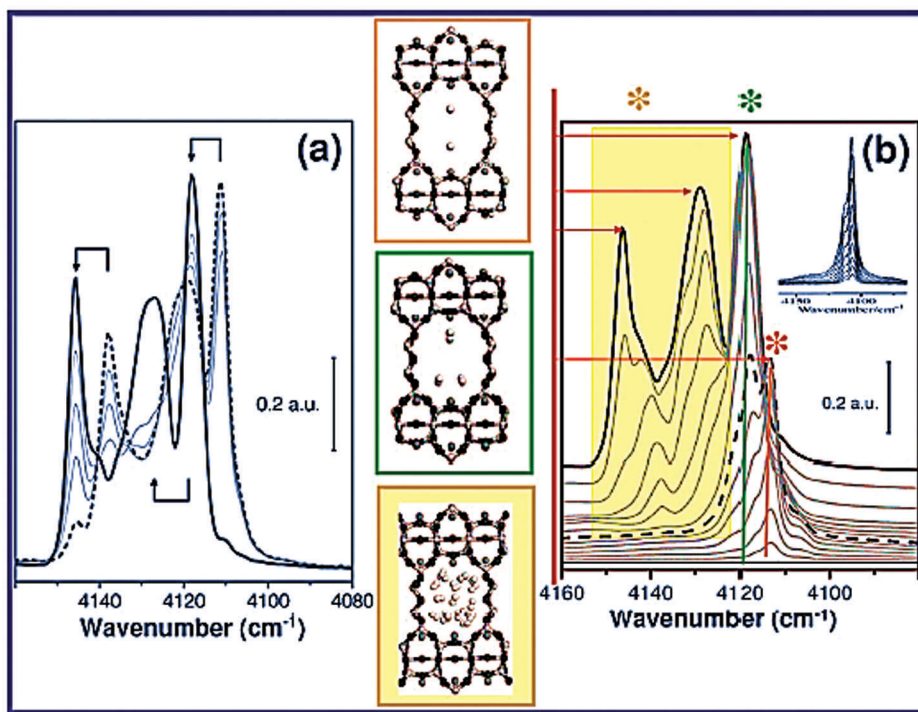


Figure 20. Fourier transform infrared spectra of H_2 adsorbed on (Na, K)-ETS (a) showing the effect of contact time (dashed line, immediately after dosage; bold line, after 10 h contact at 20 K; gray line, intermediate contact). (b) Effect of H_2 equilibrium pressure at 20 K (bold line, maximum coverage; gray curves, reducing gas pressure; dashed curve, maximum intensity of 1:1 adduct). Reproduced with permission from ref. (97) and ref. (98). Copyright 2007 Royal Society of Chemistry.

Ricchiardi et al. (97) reported adsorption of H_2 on preactivated (Na, K)-ETS-10 at 623 K for 1 h, a self-supporting thin wafer having the chemical formula $Na_{1.45}K_{0.55}TiSi_5O_{13}$ (Engelhard Corp., Iselin). The IR spectra in Figure 20a show the time evolution of dihydrogen spectra at 20 K; three intense bands appear immediately after the H_2 dosage (dashed curve). However, the intensity decreases (gray curve), showing the formation of a triplet shifted upward with time, which is completed at 10 h (solid black curve). They conclude that dihydrogen adducts are responsible for the first triplet and after transformation for the second triplet of bands (98). The spectra change showing new features with the equilibrium pressure change of dihydrogen is depicted in Figure 20b (97). Furthermore, they also studied CO adsorbed on extended surfaces and isolated surface sites. Figure 21a shows the coverage-dependent IR spectra of CO on different extended oxide and halide surfaces such as ZnO, α - Cr_2O_3 , $MgCr_2O_4$, $LaCr_2O_3$, titania, and CuCl. A coverage-dependent parameter (θ) defines the complex coverage from lowest to highest, accounting for any geometrical hindrance or lateral interaction of adsorbates resulting in shifting. For example, Zecchina et al. (98) used Degussa P25, characterized by an extremely narrow bandwidth with full width at half-maximum $<1.5\text{ cm}^{-1}$, suggesting the formation of $Ti^{4+} \dots CO$ on uniform surface planes. The surface is dominated by

electrostatic charges, which can be inferred from the shifts and dynamic polarizability. Ding et al. (99) also used IR spectroscopy to distinguish and quantify Pt single atoms from Pt nanoparticles.

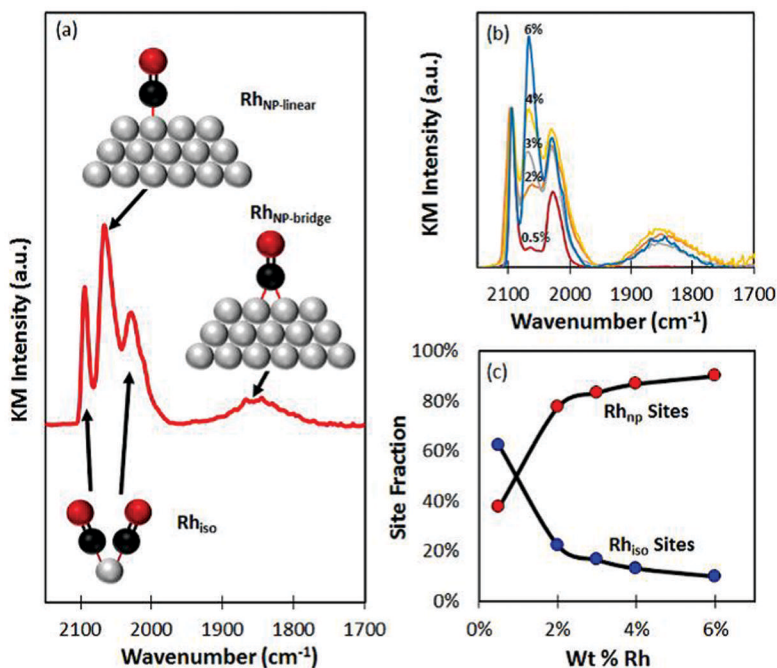


Figure 21. (a) Spectrum representing DRIFT of a saturated layer of CO adsorbed on 4%Rh/TiO₂ at 300 K along with the vibrational modes denoted by the ball and stick model. (b) CO DRIFT spectra on 0.5%, 2%, 3%, 4%, and 6% loadings of Rh/TiO₂ catalyst. (c) Percent site fraction of isolated and nanoparticle-based Rh. Reproduced with permission from ref. (100). Copyright 2015 American Chemical Society.

Other techniques such as DRIFTS having site-specific extinction coefficients can be used to quantify the fraction of metal atoms in a catalyst support from a mixture of metal atoms and nanoparticles (92, 100, 101). Matsubu et al. (100) employed probe-molecule DRIFTS to quantify the fraction of Rh dispersed to isolated sites and also on the surface of Rh nanoparticles on a TiO₂ support (Figure 21).

Thus, adsorption IR spectra of molecules such as CO can be successfully utilized to determine the electronic and structural states in various SACs. Additionally, good dispersibility of the metal catalysts can also be evaluated using these techniques, the absorption bands of which are observed at relatively higher wavenumbers.

X-ray Photoelectron Spectroscopy

X-ray photoelectron spectroscopy utilizes photoelectrons generated by X-ray irradiation (primarily Mg K α or Al K α) for surface characterization to a depth of 2–5 nm. XPS provides the elemental identification and composition by measuring electron energy on elastically scattered electron emission (102). Chemical information, including surface chemistry studies, is derived from typical binding energy peak shifts depending upon the chemical bonding of the elements.

Luo et al. (103) confirmed the presence of high contents of Au(I)-thiolate complexes in luminescent Au NCs using XPS. The XPS spectra revealed that the Au oxidation state in luminescent Au NCs resides between Au(I)-thiolate and larger Au(0) nanoparticles. The Au 4f on deconvolution

gives binding energies of 84.3 and 83.7 eV, representing the components Au(I) and Au(0), respectively. Du et al. (104) demonstrated that the electronic interaction between NCs and MoS₂ plays a key role in the highest hydrogen evolution reaction (HER) activity of Au₂Pd₆/MoS₂ compared to Pd₃/MoS₂ and Au₂/MoS₂. The Au₂Pd₆ NCs caused a large negative shift in the binding energies of Mo 3d and S 2p in Au₂Pd₆/MoS₂ than in Pd₃/MoS₂ compared to that of plain MoS₂ nanosheets. This showed the influence of the synergistic effect of the bimetallic composition in Au₂Pd₆/MoS₂ leading to improved catalytic activity. Gao et al. (105) conducted XPS measurements to examine chemical states and the effect of calcination on the prepared Pd clusters Pd₆(C₁₂H₂₅S)₁₂ symbolized by Pd₆/AC-V and Pd₆/AC. The Pd 3d in Pd₆/AC-V displayed a more positive shift in binding energy compared to Pd₆/AC, which indicates the electron cloud density is lower in Pd₆/AC-V than in Pd₆/AC. This could be attributed to the direct contact between the metal cluster and carbon support resulting in the thin carbon layers on the Pd surface after thiol ligand removal in the Pd₆/AC cluster. Zhao et al. (106) performed XPS analysis to verify successful Au₂₅ loading (with -SCH₂CH₂Ph as the ligand) onto MoS₂ nanosheets and the electronic interaction role for HER. After Au₂₅/MoS₂ formation, the binding energy of Mo 3d undergoes a negative shift of ~0.4 eV compared to bare MoS₂ with a positive shift in the binding energy of Au 5f. This suggested the transfer of electron density from Au₂₅ to MoS₂, and the electronic interaction between NCs and MoS₂ was responsible for the enhanced HER activity in Au₂₅/MoS₂ composites. Recently, the same group also performed XPS analysis to investigate the NCs and CoSe₂ interfacial interaction in enhancement of the oxygen evolution reaction (107). After the deposition of Au NCs onto the CoSe₂ support, a negative shift of ~1 eV is observed in the binding energy of Co 2p (Figure 22a), indicating the interfacial interaction between NCs and CoSe₂. This interaction is also reflected in the positive shift in the Raman peak of CoSe₂ (Figure 22b).

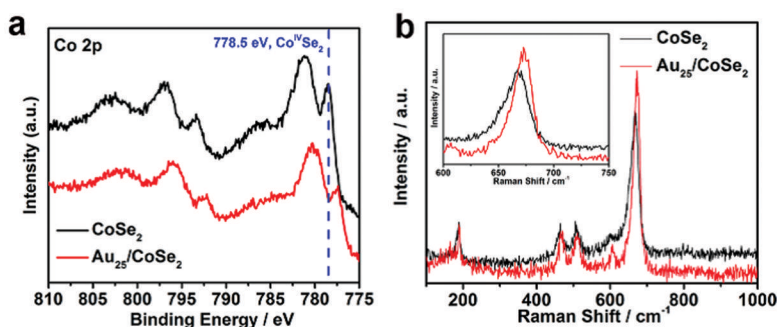


Figure 22. (a) Co 2p high-resolution XPS spectra and (b) Raman spectra of CoSe₂ and Au/CoSe₂ composite. Reproduced with permission from ref. (107). Copyright 2017 American Chemical Society.

The synergistic interaction between NCs and the support favors the intermediate (OOH) formation, resulting in facile desorption of oxygen molecules in the oxygen evolution reaction process. Hang Li et al. (108) studied the oxidation state and dispersion of Pt species using XPS analysis in PtO/TiO₂ and Pt/TiO₂ photocatalysts. For the PtO/TiO₂ catalyst, the main peaks were centered at binding energies of 72.4 and 75.8 eV, indicating the oxygen-bonded Pt 2p. The Pt/TiO₂ photocatalyst showed peaks of Pt 4f_{7/2} and 4f_{5/2} at 70.9 and 74.3 eV, respectively, justifying the

presence of metallic Pt. The Pt dispersion was evaluated on the basis of the XPS relative intensity to Ti ($I_{\text{Pt}}/I_{\text{Ti}}$). The PtO/TiO₂ showed a higher dispersion of Pt atoms, as demonstrated by their higher $I_{\text{Pt}}/I_{\text{Ti}}$ (0.021) values. These results suggest that a high oxidation state as well as high dispersity of Pt species in PtO/TiO₂ could suppress the side reaction effectively. Gaur et al. (109) reported that H₂/He-treated Au₃₈/TiO₂ exhibited excellent catalytic activity, while the air-dried Au₃₈/TiO₂ catalyst under the same conditions showed no catalytic activity. To determine the reason, XPS analysis was performed for both samples. For the reductively treated Au/TiO₂ catalyst, Au 4f_{7/2} peaks at 83.4 eV and 85.8 eV correspond to metallic Au(0) and Au(+1)-thiolate interaction, respectively. The reductive sample also showed a lower energy shift, indicating the interaction of Au atoms with an oxygen atom bonded to Ti on the surface. The XPS results showed that H₂/He-treated Au₃₈/TiO₂ removed most of the thiolate groups present, whereas the positive shift in the Au 4f peak in air-dried Au₃₈/TiO₂ was caused by the Au-SR bonding. It indicates that the thiol ligand in air-dried Au₃₈/TiO₂ inhibited Au site contact with the CO molecule, suggesting the role of the interfacial site in catalyzing the CO oxidation.

XPS is a quantitative, surface-sensitive analytical technique that provides elemental information from core levels, and the chemical composition is derived from peak shifts in nanoclusters. The XPS technique is also used to determine the chemical states of nanoclusters and to confirm the ligand removal in the calcination process. XAS and XPS are collectively used to determine the catalyst's structural integrity in the reaction. There is a large scope for improved instrumentation in terms of good energy resolution and variable X-ray energies. XPS is a highly surface-sensitive, quantitative technique that has the potential to measure the elemental composition with high quantitative precision and accuracy at the parts per thousand range. This is very crucial, especially for SAC studies, as the characterization of the individual atoms on top of the support surface is a challenging task. In conventional metal catalysts, the active sites are not well defined, so much refinement in measurement is not required. The XPS technique gives indirect evidence for successful SAC preparation by giving insight into the essential physicochemical properties of SACs. Using this technique, chemical and electronic states of an element within an SAC material can be resolved.

NMR Spectroscopy

NMR spectroscopy gives information about the structure and chemical surroundings of nanoclusters. It gives the scope to check the purity of the NCs. It helps in giving information about the estimation of binding interactions between the ligands and the metal core (52). Udayabhaskararao et al. (110) proposed the Ag thiolate structure from a cluster-based NMR spectroscopic study. The 1-D and 2-D NMR investigation of Ag₃₂SG₁₉ (SG is thiolate glutathione) showed spectral features that revealed it is dominated by the (SR-Ag-SR) structural motif.

The inner core and outer shell of the cluster with metal thiolate were explained from the detailed analysis of NMR. ¹H NMR data of clusters with chemical shifts of H3, H4, H2, H9, and H6 of glutathionate were 2.17, 2.60, 3.81, 3.87, and 4.64 ppm, respectively. H7 signals were shifted downfield (3.2–3.5 ppm) with broadening, followed by splitting denoted as [7,7] (Figure 23a). The downfield shift was due to its proximity to the silver core. The 2-D NMR data showed one pair of peaks labeled [7,7] in the ratio 1:1 at the seventh position for 2H, indicating an equivalent environment. Homonuclear correlation spectroscopy and heteronuclear single quantum correlation

were performed to find the cause of the splitting and the nature of the staple motif on the cluster surface (Figure 23b,c).

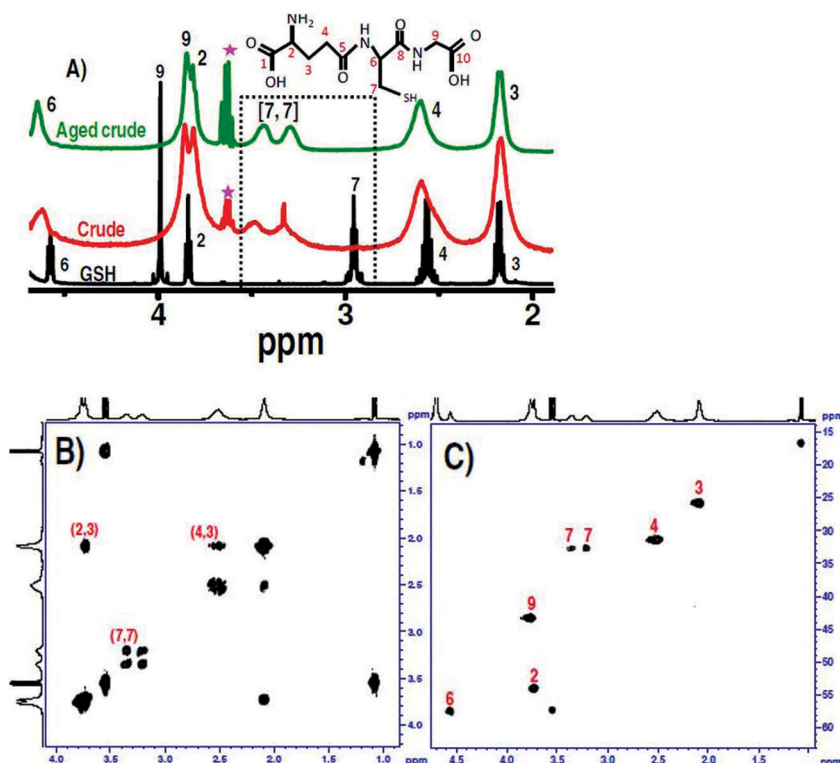


Figure 23. (a) ¹H NMR spectra of GSH, crude cluster, and aged crude; peaks inside the dotted box are due to H7. Peaks marked * at 3.6 ppm are due to residual EtOH. (b) Homonuclear correlation spectrum; (c) heteronuclear single quantum correlation spectrum. Reproduced with permission from ref. (110). Copyright 2013 Royal Society of Chemistry.

Zaluzhna et al. (111) explained the binding modes between S atoms in DMSA (meso-2,3-dimercaptosuccinic acid) and the surface Ag₇ using the ¹³C NMR spectrum. They took the ¹³C solution NMR spectrum (Figure 24) of Ag₇(DMSA)₄ NCs with free DMSA in D₂O. Here, 3-trimethylsilyl-1-propane sulfonic acid sodium salt was taken as an internal reference. It is reported (112) that the ¹³C NMR signal for carboxylate (–COO[–]) is difficult to observe due to the long spin-lattice relaxation time. In the spectra (top in Figure 24), the C bond to S appeared at 47.8 ppm in free DMSA (Figure 24). The peak disappeared once the DMSA was bound to AgNC, which is a phenomenon often observed when binding takes place between ligand and metal because of the intrinsic heterogeneity of the surface (113). The disappearance of the peak was suggested as sulfur atoms of DMSA being bound to AgNCs and that DMSA forms a bidentate binding, because if it were monodentate, one would have expected to see half of the signal at 47.8 ppm.

The nature of metal species and binding ligands during a catalytic reaction can be investigated by solid-state magic-angle spinning NMR, generally performed in situ (114). This technique has been used by Kwak et al. (115) to investigate the anchoring of Pt on alumina supports at low loading levels. Here, the surfaces that were identified to serve as the anchoring sites for Pt single atoms were

the unsaturated pentacoordinated Al^{3+} centers on the $\gamma\text{-Al}_2\text{O}_3$ support. Corma et al. (116) reported strong NMR signal enhancement due to parahydrogen-induced polarization, used to check the presence of Au single atoms. Solid-state NMR (SS NMR) is used to investigate the behavior of solid catalysts and chemical processes taking place at their surfaces (45). For example, ^{31}P SS NMR along with DFT calculations can provide information about the structure of heterogenized species and the immobilization of homogeneous metal phosphine catalysts. Gutmann et al. (117) has reported the important role of liquid and partly the SS NMR technique for the detection of surface molecules and differentiated between different binding sites on nanoscale catalysts. Mallissery et al. (118) reported the solid-state NMR of ^{31}P used to characterize phosphinine-stabilized Au NPs and a phosphinine–Au complex. Their spectra showed metal-bound, intact phosphine units and detected several surface-bound species generated by chemical transformation of the initially supplied ligands. Novio et al. (119) used SS NMR and Fourier transform infrared spectroscopy to characterize the location and dynamics of CO coordinated to Ru NPs. Ru NPs (2 nm) were tested, prepared under H_2 atmosphere, and stabilized by a bidentate phosphine ligand. The results demonstrated that CO groups were mobile on the surface of NPs, while the bulky ligand slowed down the fluxionality of CO and prevented the exchange at certain positions.

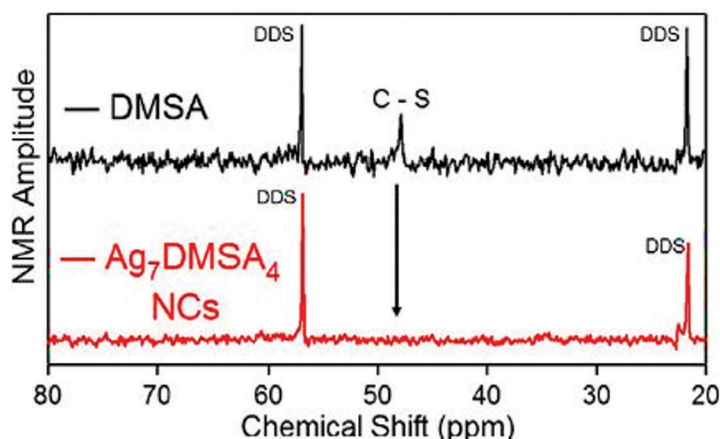


Figure 24. ^{13}C NMR spectra of free DMSA (top) and $\text{Ag}_7(\text{DMSA})_4$ NCs (bottom) in D_2O . Reproduced with permission from ref. (111). Copyright 2011 Elsevier.

MALDI-TOF-MS and Electrospray Ionization Mass Spectrometry

MALDI-TOF-MS and electrospray ionization mass spectrometry (ESI-MS) are “soft” ionization techniques as they induce minimal or no fragmentation (110). In MALDI-TOF-MS, the matrix-assisted laser desorption/ionization (MALDI) is used as an ion source, and the mass analyzer used is a time-of-flight (TOF) analyzer. Here, sample analytes are embedded in a solid matrix material, and ionized gaseous ions are formed by laser pulse irradiation (120). ESI-MS involves the conversion of solution-phase analytes into gas-phase ions by applying high voltage. Both techniques involve the generation of $[\text{M} + z\text{H}]^{z+}$ ions. Formation of singly charged species ($z = 1$) is common for MALDI, while ESI may produce multiple-charge ions ($z \gg 1$), which extends the mass analyzer range to kilodaltons to megadaltons (121). Generally, the ESI-MS technique is recommended for larger nanoclusters because of its softer ionization mode.

Qian et al. (122) confirmed the molecular purity and formula of $\text{Au}_{38}(\text{SC}_2\text{H}_4\text{Ph})_{24}$ nanoclusters using MALDI-TOF-MS and ESI-MS. An intense peak at 10,780 Da is assigned to intact $\text{Au}_{38}(\text{SC}_2\text{H}_4\text{Ph})_{24}$ ions in the MALDI spectrum with a small fragmented peak at 9342 Da (Figure 25a). The ESI technique, being a softer ionization peak, generates unfragmented Au cluster mass spectra with a sharp, intense peak at 10,910.69 Da (Figure 25b).

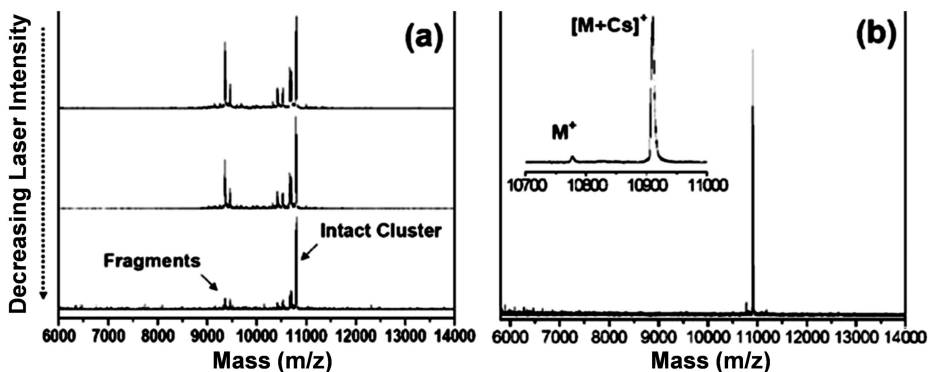


Figure 25. (a) Positive MALDI-TOF mass spectra of $\text{Au}(\text{SC}_2\text{H}_4\text{Ph})_{24}$ nanoclusters corresponding to different laser intensities (decreasing from top to bottom). (b) ESI mass spectrum of $\text{Au}(\text{SC}_2\text{H}_4\text{Ph})_{24}$; inset shows the zoomed-in spectrum. Reproduced with permission from ref. (122). Copyright 2009 American Chemical Society.

Qian et al. (123) also determined the purity of $\text{Au}_{333}(\text{SR})_{79}$ NCs using MALDI-TOF-MS and ESI-MS techniques. MALDI-MS analysis was performed using trans-2-[3-(4-tert-butylphenyl)-2-methyl-2-propenyldiene] malononitrile as a matrix. A broad peak at 75.3 kDa was observed in the MALDI-TOF-MS spectrum (Figure 26). The exact molecular mass of NPs was determined by ESI-MS analysis. Alkali acetate salt CsOAc was added to enhance nanoparticle ionization. The ESI-MS spectrum showed two sets of NP ion peaks (Figure 27), out of which the 4p ion set is chosen to precisely calculate its composition.

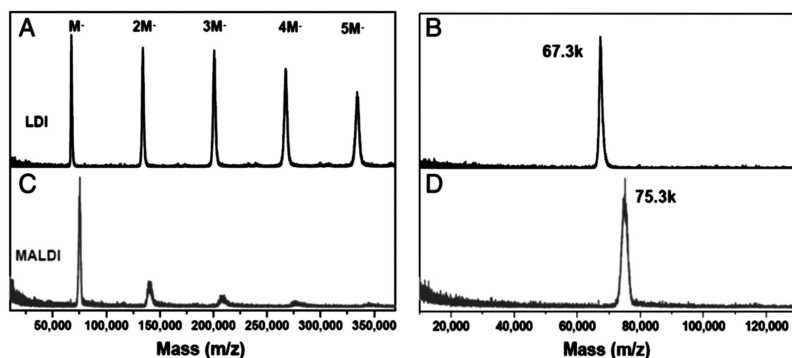


Figure 26. LDI and MALDI mass spectra of the Au nanoparticle. (A) and (C) show the spectra in the 10,000 to 370,000 range; (B) and (D) show the zoomed-in spectra. Reproduced with permission from ref. (123). Copyright 2012 National Academy of Sciences.

The mass spectrum of electrolyzed samples (Figure 28) showed a Au cluster size range of 5–13, with Au_5 (1034 Da) being the most abundant peak in these clusters. Jeyabharathi et al. (124)

synthesized CTAB-Au clusters via the electrodeposition method, and the core-size nanocluster range is identified by MALDI-TOF mass spectrometry, as shown in Figure 29. Yang et al. (125) employed MALDI-TOF-MS to confirm the actual structures of Ag NCs with a series of species with a number of atoms (two to five). Gao and Chen (105) obtained the exact formula of Pd₆ NCs via MALDI-TOF MS analysis, where the mass spectrum shows three peaks with an intense peak at $m/z = 3347$ assigned to $[\text{Pd}_6(\text{C}_{12}\text{H}_{25}\text{S})_{12} + 2\text{Na}]^+$, as shown in Figure 30.

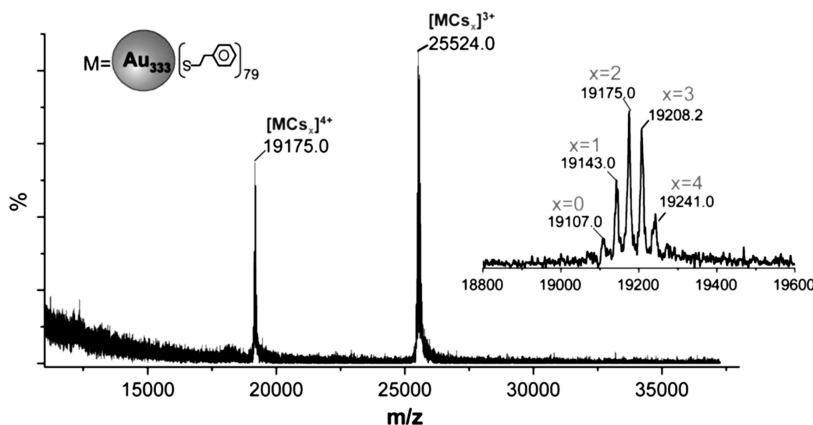


Figure 27. Wide-range ESI-MS spectrum of the nanoparticle; the inset shows the zoomed-in spectrum of the 4p ion set centered at $m/z = 19,175.0$. Reproduced with permission from ref. (123). Copyright 2012 National Academy of Sciences.

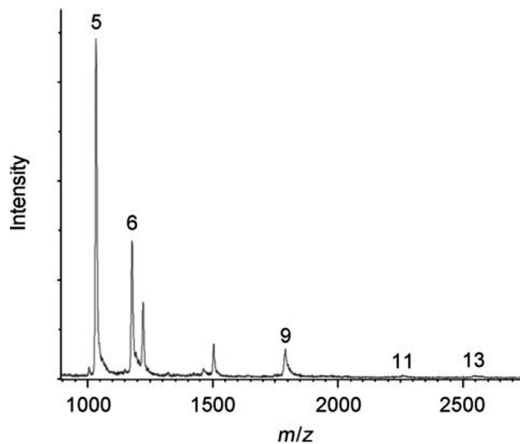


Figure 28. Au-cluster MALDI-TOF mass spectrum. Reproduced with permission from ref. (124). Copyright 2010 Wiley-VCH.

Negishi et al. (126) demonstrated the use of redox reagents for stable Au₂₅ NC formation with various charge states. The prepared Au₂₅(SC₆H₁₃)₁₈ NCs exhibited a single $[\text{Au}_{25}(\text{SC}_6\text{H}_{13})_{18}]^{1-}$ peak in the negative ESI mass spectrum, while $[\text{Au}_{25}(\text{SC}_6\text{H}_{13})_{18}]^{1-}(\text{TOA}^+)_2$ is detected in the positive ESI mass spectrum (Figure 31) with TOA⁺ as a counter ion. The $[\text{Au}_{25}(\text{SC}_6\text{H}_{13})_{18}]^{1+/-}$ ion signals were not observed in any of the ESI mass spectra, indicating the neutral $[\text{Au}_{25}(\text{SC}_6\text{H}_{13})_{18}]^0$

formation. As the reduction progresses, a shift in charge distribution of $[\text{Au}_{25}(\text{SC}_6\text{H}_{13})_{18}]^x$ to negative values was observed.

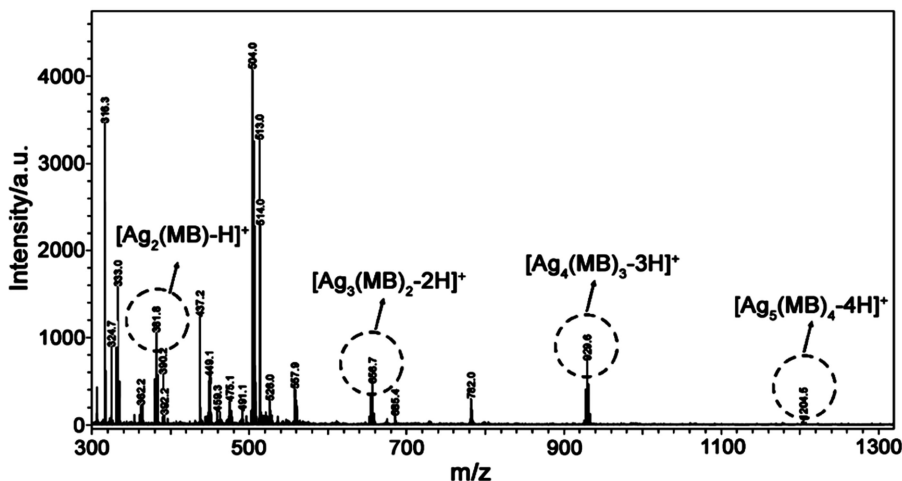


Figure 29. MALDI-TOF/TOF mass spectra of Ag NCs. Reproduced with permission from ref. (125). Copyright 2014 Royal Society of Chemistry.

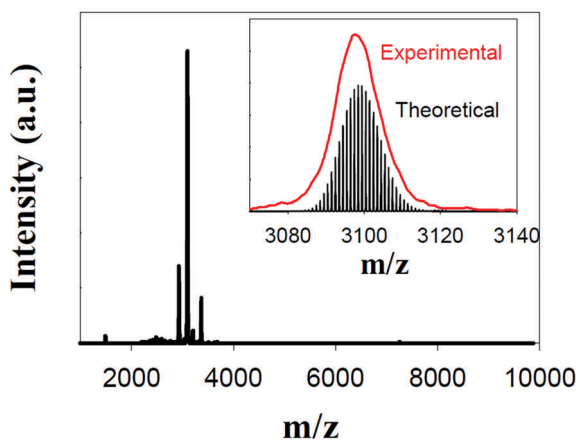


Figure 30. MALDI-TOF MS of $\text{Pd}_6(\text{C}_{12}\text{H}_{25}\text{S})_{12}$. The inset shows a comparison of the experimental and simulated patterns from the highest peak in the full spectrum. Reproduced with permission from ref. (105). Copyright 2017 Royal Society of Chemistry.

Fu et al. (127) utilized ESI-MS analysis to monitor the reaction process of the Pd_3Cl -catalyzed Suzuki–Miyaura cross-coupling reaction. It was observed that the addition of bromobenzene to the catalytic system caused the disappearance of the intermediate formed, $[\text{Pd}_3\text{Ar}(\text{PPh}_2)_2(\text{PPh}_3)_3]^+$ at 1553.11 Da, while a new peak corresponding to $[\text{Pd}_3\text{Br}(\text{PPh}_2)_2(\text{PPh}_3)_3]^+$ emerges at 1557.06 Da (Figure 32d).

Thus, we can conclude that HR-MS is a highly sensitive, selective, and reliable analytical tool used for targeted and nontargeted screening of molecular features in nanoclusters. HR-MS techniques determine the core size and composition of metallic/bimetallic nanoclusters. Using this technique, the active charge states of the nanocluster, the mixed protecting ligand composition, and the mechanism of the nanocluster formation can be identified.

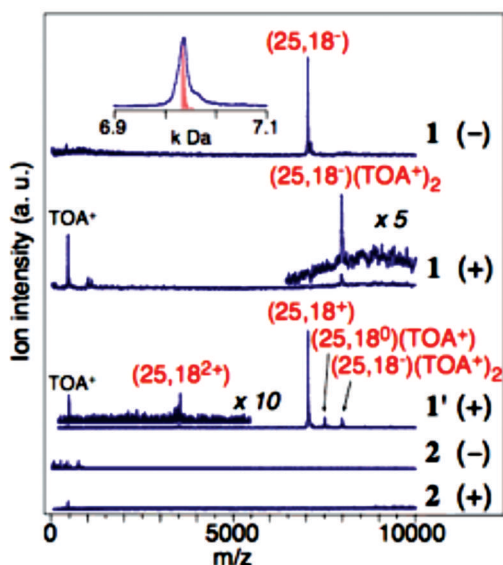


Figure 31. Positive and negative ESI mass spectra of 1, 2, and 1'. The notation $(n, m^{+/+})$ represents $[Au_n(SC_6H_{13})_m]^{+/+}$. Reproduced with permission from ref. (126). Copyright 2007 American Chemical Society.

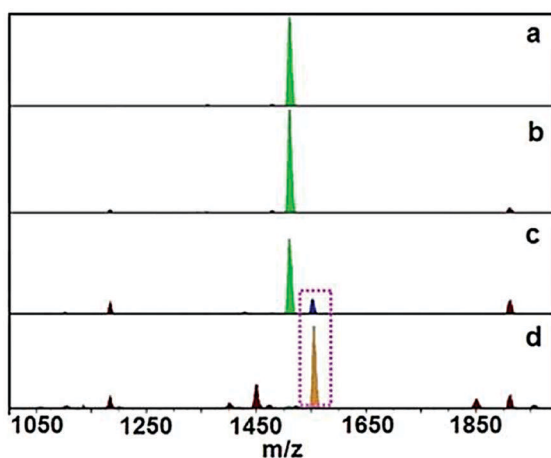


Figure 32. ESI-MS tracking of $[Pd_3Cl(PPh_2)_2(PPh_3)_3]^+$ reacting with phenylboronic acid under alkaline conditions: 0.0072 g (0.06 mmol) phenylboronic acid, 2 mg (1.32×10^{-3} mmol) catalyst, 0.0164 g (0.12 mmol) K_2CO_3 , and 3 mL CH_2Cl_2 , rt: (a) 0 h, (b) 1 h, (c) 2 h. (d) Adding 0.006 mL bromobenzene on the basis of (c). Reproduced with permission from ref. (127). Copyright 2017 American Chemical Society.

Inductively Coupled Plasma Mass Spectrometry

Inductively coupled plasma mass spectrometry (ICP-MS) is an excellent technique for determining the specific element concentration in the analyzed material with detection limits at or below the single part per trillion (ppt) level for most of the periodic table elements (128). Here, the plasma source is used to ionize the atomic elements, which are then sorted based on their mass (129). ICP-MS exhibits a species-independent high sensitivity and multielement capabilities, which allows for quantification when the species-specific standards are unavailable (130). ICP-MS

converts chromatograms into simple “elementograms”; any structural and molecular information is destroyed, so it cannot be used to elucidate structures. In such cases, ESI-MS can be used as a technique complementary to ICP-MS (131). Zhang et al. (132) employed ICP-MS for cobalt amount determination and cobalt phthalocyanine content in cobalt phthalocyanine catalysts anchored onto carbon nanotubes. Negishi et al. (133) performed ICP-MS analysis on a series of Au NCs to determine Au loading and to examine the efficiency of Au NC adsorption.

ICP-MS also helps to determine the individual isotopes of each element or isotope ratios. The isotopic ratio, in particular, is beneficial in terms of tracing and isotope dilution. Larner et al. (134) investigated the fractionation of the isotopic composition of engineered nanoparticles (ENPs), and a comparison was made concerning bulk metal material for tracing purposes. For ZnO ENPs, no fractionation of isotopic composition for ENPs was observed. Laycock et al. (135) employed ICP-MS directly to characterize stable isotope–labeled Ag ENPs for tracing studies. Degueldre and Favarger (136) introduced the application of ICP-MS in a single-particle version (SP-ICP-MS), which is based on ion cloud generation through the single particle, for engineered nanomaterial (ENM) analysis. Direct assessment of ENM size and number-size distribution is done based on the signals obtained. SP-ICP-MS has limited multielement capabilities; this has made the hyphenation of ICP-MS and the fractionation system attractive (137). Field flow fractionation (FFF) and SP-ICP-MS are complementary tools in ENM analysis. FFF-ICP-MS can fractionate nanomaterials and sensitively detect small nanomaterials by providing high resolution (Figure 33), whereas SP-ICP-MS has a unique ability to distinguish between dissolved and nanoparticulate fractions (138).

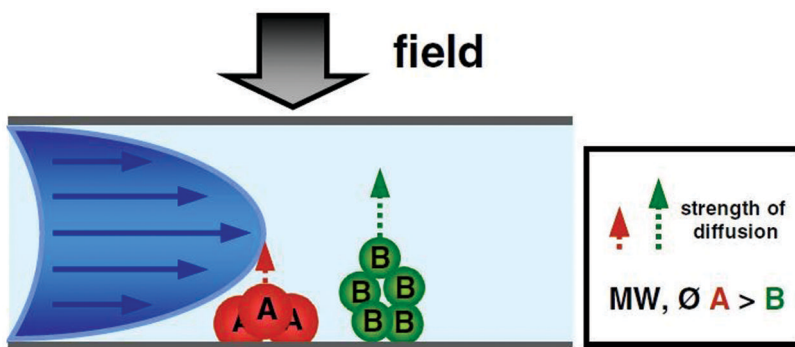


Figure 33. Simplified schematic of the separation principle of FFF. Interaction of parabolic flow-profile velocities, back diffusion of particles, and perpendicular applied field. (Scheme is not true to scale; fractionation takes place only in the lower 3–5% of the channel.). Reproduced with permission from ref. (138). Copyright 2015 Springer.

ICP-MS-based techniques are a powerful tool for metal-based single-particle and nanomaterial applications. The SP-ICP-MS technique is used for detection and quantification by measuring the elemental composition of nanomaterials. It is useful in measuring the size, number concentration, and number size distribution. If ICP-MS is coupled with hyphenated techniques such as FFF and size fractionation, the mass and number-based quantification of nanoparticles can be obtained.

Theoretical Calculations

Density functional theory calculations play an important role in the development of SACs and the specific catalytic reaction mechanisms of supported single metal atoms. Qiao et al. (13) proposed a reaction mechanism of oxidation for CO on Pt₁/FeO_x (Figure 34) based on a modified

Langmuir–Hinshelwood scheme using DFT calculations and experiments in which the active sites are single Pt atoms, coordinated with two to three oxygen atoms inserted on iron oxide.

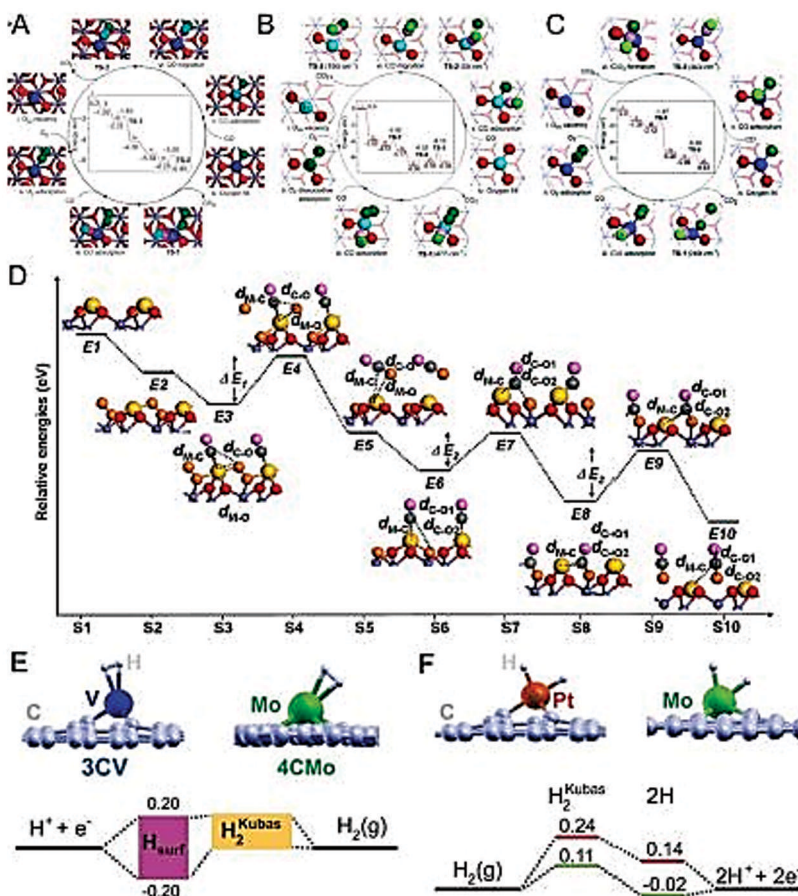


Figure 34. Proposed CO oxidation on (A) Pt₁/FeO_x. Adapted with permission from ref. (13). Copyright 2011 Nature Publishing Group. (B) Ir₁/FeO_x. Adapted with permission from ref. (139). Copyright 2014 American Chemical Society. (C) Ni₁/FeO_x catalysts. Adapted with permission from ref. (140). Copyright 2016 Royal Society of Chemistry. (D) CO oxidation on oxygen-defective M₁/FeO_x (M = Pt, Rh, Pd, Co, and Cu). Adapted with permission from ref. (141). Copyright 2015 American Chemical Society. (E) Energetic alignment (in eV) of the surface-bound H and Kubas-coordinated H intermediates for V and Mo. Adapted with permission from ref. (5). Copyright 2015 Wiley-VCH. (F) Energetic alignment (in eV) of the Kubas-coordinated H, intermediate dissociated H₂, and surface-bound H intermediates for Pt and Mo along the pathway. Reproduced with permission from ref. (33). Copyright 2019 Springer.

Here the DFT calculations suggested that single Pt atoms embedded on the surface of Fe₂O₃ show a high oxidation state as they are coordinated with two to three oxygen atoms on the surface of iron oxide, which results in a lowering of the reaction activation barrier for the rate-determining step of oxidation of CO on single Pt (0.79 eV) compared to Pt(111) (~1 eV; Figure 34a). Further, Liang et al. (139) analyzed Ir₁/FeO_x for CO oxidation using DFT, which showed that Ir₁/FeO_x has a lower activity than Pt₁/FeO_x (Figure 34b). According to the calculation, the activation barrier of the rate-determining step in the catalytic cycle of CO oxidation was 0.62 eV higher, and the adsorption

energy of the CO molecule was 0.69 eV higher for Ir₁/FeO_x than for the Pt₁/FeO_x catalyst. In addition, Liang et al. (140) using DFT predicted that Ni possessed a higher catalytic activity at room temperature for CO oxidation that was comparable to that of Pt₁/FeO_x and considerably higher than Ir₁/FeO_x, because of the lower energy barrier (Figure 34c). Later, Li et al. (141) applied DFT to explore the catalytic activity of single metal atoms supported on an iron oxide surface and reported that the performance of oxygen defective Rh₁/FeO_x, Pd₁/FeO_x, and Ru₁/FeO_x (Figure 34d) with or without O vacancies and vacancy-free Ti₁/FeO_x and Co₁/FeO_x catalyst approached the overall performance of the Pt₁/FeO_x catalyst.

DFT calculations can also be used to identify SACs. For example, Choi et al. (5) applied a computational search of hydrogen catalysts made of transition metal atoms embedded with graphitic carbon (Figure 34). Researchers have identified various materials that showed high efficiency as HER and hydrogen oxidation reaction catalysts based on numerous criteria like stability, activity, and resistance to poisoning. For example, a catalyst composed of Mo atom inserted within the divacancy site in graphene (4C Mo) was shown to be particularly promising for the hydrogen oxidation reaction catalyst in addition to HER catalyst. DFT can be used to study the molecular adsorption behavior of SACs. Lou et al. (142) anchored single Rh1 atoms to the vacancy sites of 2-D MoS₂ sheets to form Rh₁/MoS₂ SACs. Here, the DFT calculations were conducted to understand the adsorption behavior of CO molecules on edge-anchored single Rh1 atoms. The calculations suggested that such a configuration is the most stable, and under an aqueous surrounding, the most outside edge atoms of MoS₂ are the oxygen atoms. It also indicated that the Rh single atom could strongly anchor to the Mo vacancy sites to form a Rh₁-S₄ configuration (Figure 35a,b) on the edge of the nanosheets, in agreement with the HAADF-STEM observations and the EXAFS results. Also, the first-principle DFT calculations are nowadays extensively used to understand the elementary events and reaction mechanisms.

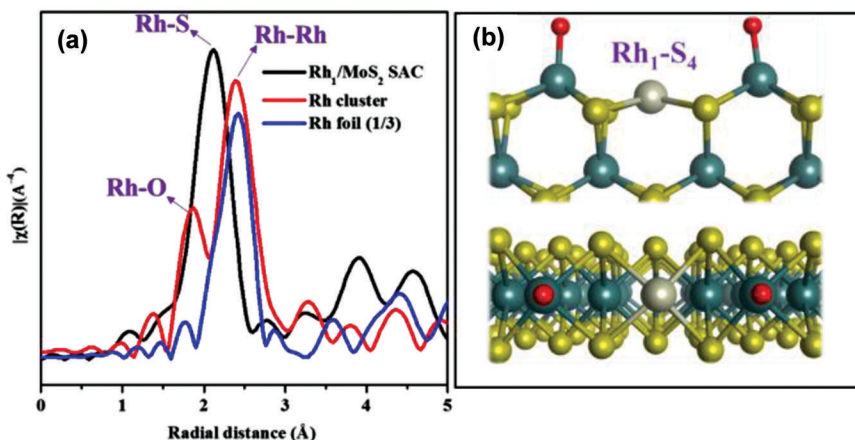


Figure 35. (a) Rh K-edge EXAFS spectra of Rh₁/MoS₂ SAC, nano-Rh/MoS₂ and Rh foil and (b) DFT-calculated stable Rh₁-S₄ configuration of the Rh₁ active site. Reproduced with permission from ref. (142).

Copyright 2019 American Chemical Society.

DFT results are converted into kinetic parameters by using transition state theory (143). However, kinetic modeling is required to check the activity and selectivity and examine the various aspects of catalytic behavior under operating conditions (144). Kopač et al. (145) investigated the

role of surface defects in catalytic CO₂ hydrogenation to methanol. Here, Cu(111) and stepped Cu(533) surfaces were compared using a multiscale modeling approach via DFT and KMC (kinetic Monte Carlo) simulations. DFT calculated the species adsorption energetics and reaction transition-state profiles. These were then used by KMC to simulate the dynamics of the overall pathway and investigate the selectivity and activity of the catalyst. The results showed that a stepped Cu(533) enhances the selectivity and activity of the methanol synthesis. Kopač et al. (146), in his other work, studied CO₂ activation for the synthesis of methanol on Cu(111) catalysts using first-principle DFT calculations and KMC modeling simulations. Huš et al. (147) used post-Hartree–Fock and DFT calculations to assess the thermodynamics and to explain the pathway leading to the synthesis of methanol from CO₂ on Cu/ZnO/Al₂O₃. On performing the DFT calculation on Cu/ZnO/Al₂O₃, it was found that the reaction proceeds via the formate route. For the development of SACs, DFT has been extensively used. It has performed various functions for the study of SACs. Examples have helped in understanding the catalytic reaction mechanism, identification of SACs, molecular adsorption studies, and so on.

Conclusion

In summary, this chapter has discussed various characterization techniques and methods used in analyzing subnano catalysts and single-atom catalysts. Understanding the materials confined at the molecular and single-atom levels, or simply the “subnanometer” level, has been one of the targets in the field of nanotechnology. This is central for analyzing the properties of this novel material and its use in different applications such as catalysis and optics. From this standpoint, many unique properties that cannot be addressed by conventional techniques due to the size and quantum effect have been discussed. We review the characterization methods: brief working principles of various major characterization techniques, the progress made so far, and the conditions required for the functioning of the analytical systems. We have discussed some of the most important tools, such as HAADF-STEM, SEM-EDAX, STM, DRIFT, other IR spectroscopy, NMR, XPS, EXAFS, TERS, ICP-MS, and X-ray reflectometry. Theoretical techniques are also fundamental in understanding the properties of these materials at the subnano level, and we review DFT as a modeling tool.

Acknowledgments

This chapter is dedicated to Prof. T. V. RajanBabu, The Ohio State University, on his 70th birthday. The authors thanks DBT-PAN IIT Centre for Bioenergy (BT/EB/PANIIT/2012) for financial assistance.

References

1. Guo, Q.; Ma, Z.; Zhou, C.; Ren, Z.; Yang, X. Single Molecule Photocatalysis on TiO₂ Surfaces. *Chem. Rev.* **2019**, *119*, 11020–11041.
2. Parkinson, G. S. Single-Atom Catalysis: How Structure Influences Catalytic Performance. *Catal. Lett.* **2019**, *149*, 1137–1146.
3. Qin, L.; Cui, Y.-Q.; Deng, T.-L.; Wei, F.-H.; Zhang, X.-F. Highly stable and Active Cu1/CeO₂ Single-Atom Catalyst for CO Oxidation: A DFT Study. *ChemPhysChem* **2018**, *19*, 3346–3349.

4. Kim, J.; Kim, H.-E.; Lee, H. Single-Atom Catalysts of Precious Metals for Electrochemical Reactions. *ChemSusChem* **2018**, *11*, 104–113.
5. Choi, W. I.; Wood, B. C.; Schwegler, E.; Ogitsu, T. Combinatorial Search for High-Activity Hydrogen Catalysts Based on Transition-Metal-Embedded Graphitic Carbons. *Adv. Energy Mater.* **2015**, *5*, 1501423.
6. Varela, M.; Findlay, S. D.; Lupini, A. R.; Christen, H. M.; Borisevich, A. Y.; Dellby, N.; Krivanek, O. L.; Nellist, P. D.; Oxley, M. P.; Allen, L. J.; Pennycook, S. J. Spectroscopic Imaging of Single Atoms within a Bulk Solid. *Phys. Rev. Lett.* **2004**, *92*, 095502.
7. Yang, X.-F.; Wang, A.; Qiao, B.; Li, J.; Liu, J.; Zhang, T. Single-Atom Catalysts: A New Frontier in Heterogeneous Catalysis. *Acc. Chem. Res.* **2013**, *46*, 1740–1748.
8. Thomas, J. M.; Raja, R.; Lewis, D. W. Single-Site Heterogeneous Catalysts. *Angew. Chem., Int. Ed.* **2005**, *44*, 6456–6482.
9. Jin, R. Quantum sized, thiolate-protected gold nanoclusters. *Nanoscale* **2010**, *2*, 343–362.
10. Alvarez, M. M.; Khoury, J. T.; Schaaff, T. G.; Shafiqullin, M. N.; Vezmar, I.; Whetten, R. L. Optical Absorption Spectra of Nanocrystal Gold Molecules. *J. Phys. Chem. B* **1997**, *101*, 3706–3712.
11. Yang, S.; Tak, Y. J.; Kim, J.; Soon, A.; Lee, H. Support Effects in Single-Atom Platinum Catalysts for Electrochemical Oxygen Reduction. *ACS Catal.* **2017**, *7*, 1301–1307.
12. Liu, J. Advanced Electron Microscopy of Metal–Support Interactions in Supported Metal Catalysts. *ChemCatChem* **2011**, *3*, 934–948.
13. Qiao, B.; Wang, A.; Yang, X.; Allard, L. F.; Jiang, Z.; Cui, Y.; Liu, J.; Li, J.; Zhang, T. Single-atom catalysis of CO oxidation using Pt1/FeOx. *Nat. Chem.* **2011**, *3*, 634–641.
14. Stroppa, D. G.; Righetto, R. D.; Montoro, L. A.; Houben, L.; Barthel, J.; Cordeiro, M. A. L.; Leite, E. R.; Weng, W.; Kiely, C. J.; Ramirez, A. J. Assessment of a nanocrystal 3-D morphology by the analysis of single HAADF-HRSTEM images. *Nanoscale Res. Lett.* **2013**, *8*, 475.
15. Chellappa, R.; Veeraraghavan, A.; Ramanathan, N.; Yam, C.-Y.; Nixon, M. S.; Elgammal, A.; Boyd, J. E.; Little, J. J.; Lynnerup, N.; Larsen, P. K.; Reynolds, D. Gaussian Mixture Models. In *Encyclopedia of Biometrics*; Springer: Boston, MA, 2009; pp 659–663.
16. McLachlan, G. J.; Peel, D. *Finite Mixtures Models*; Wiley: New York, 2000.
17. Pennycook, S. J.; Nellist, P. D., *Scanning Transmission Electron Microscopy*, 1st ed.; Springer-Verlag: New York, pp XII, 762.
18. Van Aert, S.; Verbeeck, J.; Erni, R.; Bals, S.; Luysberg, M.; Dyck, D. V.; Tendeloo, G. V. Quantitative atomic resolution mapping using high-angle annular dark field scanning transmission electron microscopy. *Ultramicroscopy* **2009**, *109*, 1236–1244.
19. Krivanek, O. L.; Chisholm, M. F.; Nicolosi, V.; Pennycook, T. J.; Corbin, G. J.; Dellby, N.; Murfitt, M. F.; Own, C. S.; Szilagyi, Z. S.; Oxley, M. P.; Pantelides, S. T.; Pennycook, S. J. Atom-by-atom structural and chemical analysis by annular dark-field electron microscopy. *Nature* **2010**, *464*, 571–574.
20. Stroppa, D. G.; Zagonel, L. F.; Montoro, L. A.; Leite, E. R.; Ramirez, A. J. High-Resolution Scanning Transmission Electron Microscopy (HRSTEM) Techniques: High-Resolution Imaging and Spectroscopy Side by Side. *ChemPhysChem* **2012**, *13*, 437–443.

21. Qiu, H.-J.; Ito, Y.; Cong, W.; Tan, Y.; Liu, P.; Hirata, A.; Fujita, T.; Tang, Z.; Chen, M. Nanoporous Graphene with Single-Atom Nickel Dopants: An Efficient and Stable Catalyst for Electrochemical Hydrogen Production. *Angew. Chem., Int. Ed.* **2015**, *54*, 14031–14035.
22. Li, X.; Bi, W.; Zhang, L.; Tao, S.; Chu, W.; Zhang, Q.; Luo, Y.; Wu, C.; Xie, Y. Single-Atom Pt as Co-Catalyst for Enhanced Photocatalytic H₂ Evolution. *Adv. Mater.* **2016**, *28*, 2427–2431.
23. Kumskov, A.; Zhigalina, V.; Kiselev, N.; Eliseev, A.; Verbitskiy, N.; Vasiliev, A. HAADF HRSTEM of one dimensional CuI crystals inside SWCNTs. In *European Microscopy Congress 2016: Proceedings*; Wiley-VCH, pp 490–491.
24. Zhang, Z.; Zhu, Y.; Asakura, H.; Zhang, B.; Zhang, J.; Zhou, M.; Han, Y.; Tanaka, T.; Wang, A.; Zhang, T.; Yan, N. Thermally stable single atom Pt/m-Al₂O₃ for selective hydrogenation and CO oxidation. *Nat. Commun.* **2017**, *8*, 16100.
25. Liu, Q.; Zhang, Z. Platinum single-atom catalysts: a comparative review towards effective characterization. *Catal. Sci. Technol.* **2019**, *9*, 4821–4834.
26. Liu, L.; Zakharov, D. N.; Arenal, R.; Concepcion, P.; Stach, E. A.; Corma, A. Evolution and stabilization of subnanometric metal species in confined space by in situ TEM. *Nat. Commun.* **2018**, *9*, 574.
27. Wiesendanger, R. Single-atom magnetometry. *Curr. Opin. Solid State Mater. Sci.* **2011**, *15*, 1–7.
28. Ternes, M.; Heinrich, A. J.; Schneider, W.-D. Spectroscopic manifestations of the Kondo effect on single adatoms. *J. Phys. Condens. Matter* **2008**, *21*, 053001.
29. Zhou, X.; Yang, W.; Chen, Q.; Geng, Z.; Shao, X.; Li, J.; Wang, Y.; Dai, D.; Chen, W.; Xu, G.; Yang, X.; Wu, K. Stable Pt Single Atoms and Nanoclusters on Ultrathin CuO Film and Their Performances in CO Oxidation. *J. Phys. Chem. C* **2016**, *120*, 1709–1715.
30. Krenner, W.; Klappenberger, F.; Kühne, D.; Diller, K.; Qu, Z.-R.; Ruben, M.; Barth, J. V. Positioning of Single Co Atoms Steered by a Self-Assembled Organic Molecular Template. *J. Phys. Chem. Lett.* **2011**, *2*, 1639–1645.
31. Lucci, F. R.; Liu, J.; Marcinkowski, M. D.; Yang, M.; Allard, L. F.; Flytzani-Stephanopoulos, M.; Sykes, E. C. H. Selective hydrogenation of 1,3-butadiene on platinum–copper alloys at the single-atom limit. *Nat. Commun.* **2015**, *6*, 8550.
32. Boucher, M. B.; Goergen, S.; Yi, N.; Flytzani-Stephanopoulos, M. ‘Shape effects’ in metal oxide supported nanoscale gold catalysts. *Phys. Chem. Chem. Phys.* **2011**, *13*, 2517–2527.
33. Cheng, N.; Zhang, L.; Doyle-Davis, K.; Sun, X. Single-Atom Catalysts: From Design to Application. *Electrochem. Energy Rev.* **2019**, *2*, 539–573.
34. Venkatachalam, S.; Jacob, T. Hydrogen adsorption on Pd-containing Au(111) bimetallic surfaces. *Phys. Chem. Chem. Phys.* **2009**, *11*, 3263–3270.
35. Yudanov, I. V.; Neyman, K. M. Stabilization of Au at edges of bimetallic PdAu nanocrystallites. *Phys. Chem. Chem. Phys.* **2010**, *12*, 5094–5100.
36. Yuan, D.; Gong, X.; Wu, R. Atomic configurations of Pd atoms in PdAu(111) bimetallic surfaces investigated using the first-principles pseudopotential plane wave approach. *Phys. Rev. B* **2007**, *75*, 085428.
37. Baber, A. E.; Tierney, H. L.; Sykes, E. C. H. Atomic-Scale Geometry and Electronic Structure of Catalytically Important Pd/Au Alloys. *ACS Nano* **2010**, *4*, 1637–1645.

38. Lucci, F. R.; Darby, M. T.; Mattera, M. F. G.; Ivimey, C. J.; Therrien, A. J.; Michaelides, A.; Stamatakis, M.; Sykes, E. C. H. Controlling Hydrogen Activation, Spillover, and Desorption with Pd–Au Single-Atom Alloys. *J. Phys. Chem. Lett.* **2016**, *7*, 480–485.
39. Liu, J.; Lucci, F. R.; Yang, M.; Lee, S.; Marcinkowski, M. D.; Therrien, A. J.; Williams, C. T.; Sykes, E. C. H.; Flytzani-Stephanopoulos, M. Tackling CO Poisoning with Single-Atom Alloy Catalysts. *J. Am. Chem. Soc.* **2016**, *138*, 6396–6399.
40. Wang, Y.; Mao, J.; Meng, X.; Yu, L.; Deng, D.; Bao, X. Catalysis with Two-Dimensional Materials Confining Single Atoms: Concept, Design, and Applications. *Chem. Rev.* **2019**, *119*, 1806–1854.
41. Deng, D.; Pan, X.; Yu, L.; Cui, Y.; Jiang, Y.; Qi, J.; Li, W.-X.; Fu, Q.; Ma, X.; Xue, Q.; Sun, G.; Bao, X. Toward N-Doped Graphene via Solvothermal Synthesis. *Chem. Mater.* **2011**, *23*, 1188–1193.
42. Zheng, B.; Hermet, P.; Henrard, L. Scanning Tunneling Microscopy Simulations of Nitrogen- and Boron-Doped Graphene and Single-Walled Carbon Nanotubes. *ACS Nano* **2010**, *4*, 4165–4173.
43. Zhao, L.; He, R.; Rim, K. T.; Schiros, T.; Kim, K. S.; Zhou, H.; Gutiérrez, C.; Chockalingam, S. P.; Arguello, C. J.; Pálková, L.; Nordlund, D.; Hybertsen, M. S.; Reichman, D. R.; Heinz, T. F.; Kim, P.; Pinczuk, A.; Flynn, G. W.; Pasupathy, A. N. Visualizing Individual Nitrogen Dopants in Monolayer Graphene. *Science* **2011**, *333*, 999–1003.
44. Binnig, G.; Rohrer, H. Scanning tunneling microscopy---From birth to adolescence. *Rev. Mod. Phys.* **1987**, *59*, 615–625.
45. Mourdikoudis, S.; Pallares, R. M.; Thanh, N. T. K. Characterization techniques for nanoparticles: Comparison and complementarity upon studying nanoparticle properties. *Nanoscale* **2018**, *10*, 12871–12934.
46. Girão, A. V.; Caputo, G.; Ferro, M. C. Chapter 6, Application of Scanning Electron Microscopy–Energy Dispersive X-Ray Spectroscopy (SEM-EDS). In *Comprehensive Analytical Chemistry*; Rocha-Santos, T. A. P., Duarte, A. C., Eds.; Elsevier: 2017; Vol. 75, pp 153–168.
47. Tang, Y.; Yang, Y.; Cheng, D.; Gao, B.; Wan, Y.; Li, Y. C. Value-Added Humic Acid Derived from Lignite Using Novel Solid-Phase Activation Process with Pd/CeO₂ Nanocatalyst: A Physicochemical Study. *ACS Sustainable Chem. Eng.* **2017**, *5*, 10099–10110.
48. Han, W.; Zhang, C.; Wang, H.; Zhou, S.; Tang, H.; Yang, L.; Wang, Z. Sub-nano MgF₂ embedded in carbon nanofibers and electrospun MgF₂ nanofibers by one-step electrospinning as highly efficient catalysts for 1,1,1-trifluoroethane dehydrofluorination. *Catal. Sci. Technol.* **2017**, *7*, 6000–6012.
49. Klaysri, R.; Preechawan, V.; Thammachai, N.; Praserttham, P.; Mekasuwandumrong, O. Photocatalytic activity of Nitrogen and Silica doping on TiO₂ nanocatalyst and grafted onto PMMA film. *Mater. Chem. Phys.* **2018**, *211*, 420–427.
50. Pascariu, P.; Tudose, I. V.; Suche, M.; Koudoumas, E.; Fifer, N.; Airinei, A. Preparation and characterization of Ni, Co doped ZnO nanoparticles for photocatalytic applications. *Appl. Surf. Sci.* **2018**, *448*, 481–488.
51. Blass, S. D.; Hermann, R. J.; Persson, N. E.; Bhan, A.; Schmidt, L. D. Conversion of glycerol to light olefins and gasoline precursors. *Appl. Catal., A* **2014**, *475*, 10–15.

52. Du, Y.; Sheng, H.; Astruc, D.; Zhu, M. Atomically Precise Noble Metal Nanoclusters as Efficient Catalysts: A Bridge between Structure and Properties. *Chem. Rev.* **2020**, *120*, 526–622.
53. Nadjia, L.; Abdelkader, E.; Naceur, B.; Ahmed, B. CeO₂ nanoscale particles: Synthesis, characterization and photocatalytic activity under UVA light irradiation. *J. Rare Earth* **2018**, *36*, 575–587.
54. Wang, Z. L.; Lee, J. L., 9: Electron Microscopy Techniques for Imaging and Analysis of Nanoparticles. In *Developments in Surface Contamination and Cleaning*; Kohli, R., Mittal, K. L., Eds.; William Andrew Publishing: Norwich, NY, 2008; pp 531–584.
55. Mahajan, A.; Banik, S.; Roy, P. S.; Chowdhury, S. R.; Bhattacharya, S. K. Kinetic parameters of anodic oxidation of methanol in alkali: Effect of diameter of Pd nano-catalyst, composition of electrode and solution and mechanism of the reaction. *Int. J. Hydrogen Energy* **2017**, *42*, 21263–21278.
56. Ganeev, R. A.; Suzuki, M.; Baba, M.; Ichihara, M.; Kuroda, H. Low- and high-order nonlinear optical properties of BaTiO₃ and SrTiO₃ nanoparticles. *J. Opt. Soc. Am. B* **2008**, *25*, 325–333.
57. Rahman, T.; Borah, G.; Gogoi, P. K. Spinel Structured Copper Ferrite Nano Catalyst with Magnetic Recyclability for Oxidative Decarboxylation of Phenyl Acetic Acids. *Catal. Lett.* **2020**, *150*, 2267–2272.
58. Khazaei, A.; Jafari-Ghalebakhani, L.; Ghaderi, E.; Tavasoli, M.; Moosavi-Zare, A. R. Synthesis, characterization and application of nano-CoAl₂O₄ as an efficient catalyst in the preparation of hexahydroquinolines. *Appl. Organomet. Chem.* **2017**, *31*, e3815.
59. Valan, M. F.; Manikandan, A.; Antony, S. A. Microwave Combustion Synthesis and Characterization Studies of Magnetic Zn(1-x)Cd(x)Fe₂O₄ (0 ≤ x ≤ 0.5) Nanoparticles. *J. Nanosci. Nanotechnol.* **2015**, *15*, 4543–51.
60. Park, K.-D.; Raschke, M. B.; Atkin, J. M.; Lee, Y. H.; Jeong, M. S. Probing Bilayer Grain Boundaries in Large-Area Graphene with Tip-Enhanced Raman Spectroscopy. *Adv. Mater.* **2017**, *29*, 1603601.
61. Chiang, N.; Chen, X.; Goubert, G.; Chulhai, D. V.; Chen, X.; Pozzi, E. A.; Jiang, N.; Hersam, M. C.; Seideman, T.; Jensen, L.; Van Duyne, R. P. Conformational Contrast of Surface-Mediated Molecular Switches Yields Angstrom-Scale Spatial Resolution in Ultrahigh Vacuum Tip-Enhanced Raman Spectroscopy. *Nano Lett.* **2016**, *16*, 7774–7778.
62. Shao, F.; Zenobi, R. Tip-enhanced Raman spectroscopy: principles, practice, and applications to nanospectroscopic imaging of 2D materials. *Anal. Bioanal. Chem.* **2019**, *411*, 37–61.
63. Liu, S.; Müller, M.; Sun, Y.; Hamada, I.; Hammud, A.; Wolf, M.; Kumagai, T. Resolving the Correlation between Tip-Enhanced Resonance Raman Scattering and Local Electronic States with 1 nm Resolution. *Nano Lett.* **2019**, *19*, 5725–5731.
64. Balois, M. V.; Hayazawa, N.; Yasuda, S.; Ikeda, K.; Yang, B.; Kazuma, E.; Yokota, Y.; Kim, Y.; Tanaka, T. Visualization of subnanometric phonon modes in a plasmonic nano-cavity via ambient tip-enhanced Raman spectroscopy. *NPJ 2D Mater. Appl.* **2019**, *3*, 38.
65. Ichimura, T.; Fujii, S.; Verma, P.; Yano, T.; Inouye, Y.; Kawata, S. Subnanometric Near-Field Raman Investigation in the Vicinity of a Metallic Nanostructure. *Phys. Rev. Lett.* **2009**, *102*, 186101.

66. Cleveland, J. P.; Anczykowski, B.; Schmid, A. E.; Elings, V. B. Energy dissipation in tapping-mode atomic force microscopy. *Appl. Phys. Lett.* **1998**, *72*, 2613–2615.
67. Zhang, R.; Zhang, Y.; Dong, Z. C.; Jiang, S.; Zhang, C.; Chen, L. G.; Zhang, L.; Liao, Y.; Aizpurua, J.; Luo, Y.; Yang, J. L.; Hou, J. G. Chemical mapping of a single molecule by plasmon-enhanced Raman scattering. *Nature* **2013**, *498*, 82–86.
68. Stipe, B. C.; Rezaei, M. A.; Ho, W. Single-Molecule Vibrational Spectroscopy and Microscopy. *Science* **1998**, *280*, 1732–1735.
69. Richard-Lacroix, M.; Zhang, Y.; Dong, Z.; Deckert, V. Mastering high resolution tip-enhanced Raman spectroscopy: towards a shift of perception. *Chem. Soc. Rev.* **2017**, *46*, 3922–3944.
70. Szwedowski-Rammert, V.; Baumann, J.; Schlesiger, C.; Waldschläger, U.; Gross, A.; Kanngießer, B.; Mantouvalou, I. Laboratory based GIXRF and GEXRF spectrometers for multilayer structure investigations. *J. Anal. At. Spectrom.* **2019**, *34*, 922–929.
71. Mao, P. H.; Harrison, F. A.; Windt, D. L.; Christensen, F. E. Optimization of graded multilayer designs for astronomical X-ray telescopes. *Appl. Opt.* **1999**, *38*, 4766–4775.
72. Ménesguen, Y.; de Rossi, S.; Meltchakov, E.; Delmotte, F. Aperiodic multilayer mirrors for efficient broadband reflection in the extreme ultraviolet. *Appl. Phys. A* **2009**, *98*, 305.
73. Bridou, F.; Delmotte, F.; Troussel, P.; Villette, B. Design and fabrication of X-ray non-periodic multilayer mirrors: Apodization and shaping of their spectral response. *Nucl. Instrum. Meth. A* **2012**, *680*, 69–74.
74. Ingerle, D.; Schiebl, M.; Strel, C.; Wobrauschek, P. Combination of grazing incidence X-ray fluorescence with X-ray reflectivity in one table-top spectrometer for improved characterization of thin layer and implants on/in silicon wafers. *Rev. Sci. Instrum.* **2014**, *85*, 083110.
75. Hönicke, P.; Detlefs, B.; Müller, M.; Darlatt, E.; Nolot, E.; Grampeix, H.; Beckhoff, B. Reference-free, depth-dependent characterization of nanolayers and gradient systems with advanced grazing incidence X-ray fluorescence analysis. *Phys. Status Solidi A* **2015**, *212*, 523–528.
76. Parratt, L. G.; Hempstead, C. F. Anomalous Dispersion and Scattering of X-Rays. *Phys. Rev.* **1954**, *94*, 1593–1600.
77. Beckhoff, B. Reference-free X-ray spectrometry based on metrology using synchrotron radiation. *J. Anal. At. Spectrom.* **2008**, *23*, 845–853.
78. Emprin, B.; Troussel, P.; Soullié, G.; Stemmler, P.; Mercère, P.; Meltchakov, E.; Jérôme, A.; Delmotte, F. Characterization of subnanometric layers by grazing incidence X-ray reflectometry. *Thin Solid Films* **2014**, *556*, 54–60.
79. Haase, A.; Bajt, S.; Hönicke, P.; Soltwisch, V.; Scholze, F. Multiparameter characterization of subnanometre Cr/Sc multilayers based on complementary measurements. *J. Appl. Crystallogr.* **2016**, *49*, 2161–2171.
80. Zhang, P. X-ray Spectroscopy of Gold–Thiolate Nanoclusters. *J. Phys. Chem. C* **2014**, *118*, 25291–25299.
81. Jin, R.; Zeng, C.; Zhou, M.; Chen, Y. Atomically Precise Colloidal Metal Nanoclusters and Nanoparticles: Fundamentals and Opportunities. *Chem. Rev.* **2016**, *116*, 10346–10413.
82. MacDonald, M. A.; Zhang, P.; Qian, H.; Jin, R. Site-Specific and Size-Dependent Bonding of Compositionally Precise Gold–Thiolate Nanoparticles from X-ray Spectroscopy. *J. Phys. Chem. Lett.* **2010**, *1*, 1821–1825.

83. MacDonald, M. A.; Zhang, P.; Chen, N.; Qian, H.; Jin, R. Solution-Phase Structure and Bonding of Au₃₈(SR)₂₄ Nanoclusters from X-ray Absorption Spectroscopy. *J. Phys. Chem. C* **2011**, *115*, 65–69.
84. MacDonald, M. A.; Chevrier, D. M.; Zhang, P.; Qian, H.; Jin, R. The Structure and Bonding of Au₂₅(SR)₁₈ Nanoclusters from EXAFS: The Interplay of Metallic and Molecular Behavior. *J. Phys. Chem. C* **2011**, *115*, 15282–15287.
85. Christensen, S. L.; MacDonald, M. A.; Chatt, A.; Zhang, P.; Qian, H.; Jin, R. Dopant Location, Local Structure, and Electronic Properties of Au₂₄Pt(SR)₁₈ Nanoclusters. *J. Phys. Chem. C* **2012**, *116*, 26932–26937.
86. Chevrier, D. M.; MacDonald, M. A.; Chatt, A.; Zhang, P.; Wu, Z.; Jin, R. Sensitivity of Structural and Electronic Properties of Gold–Thiolate Nanoclusters to the Atomic Composition: A Comparative X-ray Study of Au₁₉(SR)₁₃ and Au₂₅(SR)₁₈. *J. Phys. Chem. C* **2012**, *116*, 25137–25142.
87. Chevrier, D. M.; Chatt, A.; Zhang, P.; Zeng, C.; Jin, R. Unique Bonding Properties of the Au₃₆(SR)₂₄ Nanocluster with FCC-Like Core. *J. Phys. Chem. Lett.* **2013**, *4*, 3186–3191.
88. Zhang, F.; Jiao, F.; Pan, X.; Gao, K.; Xiao, J.; Zhang, S.; Bao, X. Tailoring the Oxidation Activity of Pt Nanoclusters via Encapsulation. *ACS Catal.* **2015**, *5*, 1381–1385.
89. Yamazoe, S.; Takano, S.; Kurashige, W.; Yokoyama, T.; Nitta, K.; Negishi, Y.; Tsukuda, T. Hierarchy of bond stiffnesses within icosahedral-based gold clusters protected by thiolates. *Nat. Commun.* **2016**, *7*, 10414.
90. Ryczkowski, J. IR spectroscopy in catalysis. *Catal. Today* **2001**, *68*, 263–381.
91. Lamberti, C.; Zecchina, A.; Groppo, E.; Bordiga, S. Probing the surfaces of heterogeneous catalysts by in situ IR spectroscopy. *Chem. Soc. Rev.* **2010**, *39*, 4951–5001.
92. Liu, J. Catalysis by Supported Single Metal Atoms. *ACS Catal.* **2017**, *7*, 34–59.
93. Lamberti, C.; Groppo, E.; Spoto, G.; Bordiga, S.; Zecchina, A., Infrared Spectroscopy of Transient Surface Species. In *Advances in Catalysis*; Gates, B. C., Knözinger, H., Eds.; Academic Press: Cambridge, MA, 2007; Vol. 51, pp 1–74.
94. Hülsey, M. J.; Zhang, B.; Ma, Z.; Asakura, H.; Do, D. A.; Chen, W.; Tanaka, T.; Zhang, P.; Wu, Z.; Yan, N. In situ spectroscopy-guided engineering of rhodium single-atom catalysts for CO oxidation. *Nat. Commun.* **2019**, *10*, 1330.
95. Li, X.; Yang, X.; Zhang, J.; Huang, Y.; Liu, B. In Situ/Operando Techniques for Characterization of Single-Atom Catalysts. *ACS Catal.* **2019**, *9*, 2521–2531.
96. Yan, H.; Su, C.; He, J.; Chen, W. Single-atom catalysts and their applications in organic chemistry. *J. Mater. Chem. A* **2018**, *6*, 8793–8814.
97. Ricchiardi, G.; Vitillo, J. G.; Cocina, D.; Gribov, E. N.; Zecchina, A. Direct observation and modelling of ordered hydrogen adsorption and catalyzed ortho–para conversion on ETS-10 titanosilicate material. *Phys. Chem. Chem. Phys.* **2007**, *9*, 2753–2760.
98. Zecchina, A.; Otero Areán, C.; Turnes Palomino, G.; Geobaldo, F.; Lamberti, C.; Spoto, G.; Bordiga, S. The vibrational spectroscopy of H₂, N₂, CO and NO adsorbed on the titanosilicate molecular sieve ETS-10. *Phys. Chem. Chem. Phys.* **1999**, *1*, 1649–1657.
99. Ding, K.; Gulec, A.; Johnson, A. M.; Schweitzer, N. M.; Stucky, G. D.; Marks, L. D.; Stair, P. C. Identification of active sites in CO oxidation and water-gas shift over supported Pt catalysts. *Science* **2015**, *350*, 189–192.

100. Matsubu, J. C.; Yang, V. N.; Christopher, P. Isolated Metal Active Site Concentration and Stability Control Catalytic CO₂ Reduction Selectivity. *J. Am. Chem. Soc.* **2015**, *137*, 3076–3084.
101. Manzoli, M. Boosting the Characterization of Heterogeneous Catalysts for H₂O₂ Direct Synthesis by Infrared Spectroscopy. *Catalysts* **2019**, *9*, 30.
102. X-Ray Photoelectron Spectroscopy in Analysis of Surfaces. Update based on the original article by Steffen Oswald, Encyclopedia of Analytical Chemistry, 2000, John Wiley & Sons, Ltd. In *Encyclopedia of Analytical Chemistry*.
103. Luo, Z.; Yuan, X.; Yu, Y.; Zhang, Q.; Leong, D. T.; Lee, J. Y.; Xie, J. From Aggregation-Induced Emission of Au(I)–Thiolate Complexes to Ultrabright Au(0)@Au(I)–Thiolate Core–Shell Nanoclusters. *J. Am. Chem. Soc.* **2012**, *134*, 16662–16670.
104. Du, Y.; Xiang, J.; Ni, K.; Yun, Y.; Sun, G.; Yuan, X.; Sheng, H.; Zhu, Y.; Zhu, M. Design of atomically precise Au₂Pd₆ nanoclusters for boosting electrocatalytic hydrogen evolution on MoS₂. *Inorg. Chem. Front.* **2018**, *5*, 2948–2954.
105. Gao, X.; Chen, W. Highly stable and efficient Pd₆(SR)₁₂ cluster catalysts for the hydrogen and oxygen evolution reactions. *ChemComm* **2017**, *53*, 9733–9736.
106. Zhao, S.; Jin, R.; Song, Y.; Zhang, H.; House, S. D.; Yang, J. C.; Jin, R. Atomically Precise Gold Nanoclusters Accelerate Hydrogen Evolution over MoS₂ Nanosheets: The Dual Interfacial Effect. *Small* **2017**, *13*, 1701519.
107. Zhao, S.; Jin, R.; Abroshan, H.; Zeng, C.; Zhang, H.; House, S. D.; Gottlieb, E.; Kim, H. J.; Yang, J. C.; Jin, R. Gold Nanoclusters Promote Electrocatalytic Water Oxidation at the Nanocluster/CoSe₂ Interface. *J. Am. Chem. Soc.* **2017**, *139*, 1077–1080.
108. Hang Li, Y.; Xing, J.; Jia Chen, Z.; Li, Z.; Tian, F.; Rong Zheng, L.; Feng Wang, H.; Hu, P.; Jun Zhao, H.; Gui Yang, H. Unidirectional suppression of hydrogen oxidation on oxidized platinum clusters. *Nat. Commun.* **2013**, *4*, 2500.
109. Gaur, S.; Miller, J. T.; Stellwagen, D.; Sanampudi, A.; Kumar, C. S. S. R.; Spivey, J. J. Synthesis, characterization, and testing of supported Au catalysts prepared from atomically-tailored Au₃₈(SC₁₂H₂₅)₂₄ clusters. *Phys. Chem. Chem. Phys.* **2012**, *14*, 1627–1634.
110. Udayabhaskararao, T.; Bootharaju, M. S.; Pradeep, T. Thiolate-protected Ag₃₂ clusters: mass spectral studies of composition and insights into the Ag–thiolate structure from NMR. *Nanoscale* **2013**, *5*, 9404–9411.
111. Zaluzhna, O.; Brightful, L.; Allison, T. C.; Tong, Y. J. Spectroscopic evidence of a bidentate-binding of meso-2,3-dimercaptosuccinic acid on silver nanoclusters. *Chem. Phys. Lett.* **2011**, *509*, 148–151.
112. Nishiyama, N.; Suzuki, K.; Komatsu, K.; Yasuda, S.; Nemoto, K. A ¹³C NMR Study on the Adsorption Characteristics of HEMA to Dentinal Collagen. *J. Dent. Res.* **2002**, *81*, 469–471.
113. Lica, G. C.; Zelakiewicz, B. S.; Tong, Y. Y. Electrochemical and NMR characterization of octanethiol-protected Au nanoparticles. *J. Electroanal. Chem.* **2003**, *554–555*, 127–132.
114. Zhang, W.; Xu, S.; Han, X.; Bao, X. In situ solid-state NMR for heterogeneous catalysis: a joint experimental and theoretical approach. *Chem. Soc. Rev.* **2012**, *41*, 192–210.

115. Kwak, J. H.; Hu, J.; Mei, D.; Yi, C.-W.; Kim, D. H.; Peden, C. H. F.; Allard, L. F.; Szanyi, J. Coordinatively Unsaturated Al³⁺ Centers as Binding Sites for Active Catalyst Phases of Platinum on γ -Al₂O₃. *Science* **2009**, *325*, 1670–1673.
116. Corma, A.; Salnikov, O. G.; Barskiy, D. A.; Kovtunov, K. V.; Koptuyug, I. V. Single-Atom Gold Catalysis in the Context of Developments in Parahydrogen-Induced Polarization. *Chem. - Eur. J.* **2015**, *21*, 7012–7015.
117. Gutmann, T.; Grünberg, A.; Rothermel, N.; Werner, M.; Srou, M.; Abdulhussain, S.; Tan, S.; Xu, Y.; Breitzke, H.; Buntkowsky, G. Solid-state NMR concepts for the investigation of supported transition metal catalysts and nanoparticles. *Solid State Nucl. Magn. Reson.* **2013**, *55–56*, 1–11.
118. Malliserry, S. K.; Gudat, D. Solid-state ³¹P NMR characterisation of phosphinine-stabilised gold nanoparticles and a phosphinine-gold complex. *Dalton Trans.* **2010**, *39*, 4280–4284.
119. Novio, F.; Philippot, K.; Chaudret, B. Location and Dynamics of CO Co-ordination on Ru Nanoparticles: A Solid State NMR Study. *Catal. Lett.* **2010**, *140*, 1–7.
120. Dass, A.; Stevenson, A.; Dubay, G. R.; Tracy, J. B.; Murray, R. W. Nanoparticle MALDI-TOF Mass Spectrometry without Fragmentation: Au₂₅(SCH₂CH₂Ph)₁₈ and Mixed Monolayer Au₂₅(SCH₂CH₂Ph)_{18-x}(L)_x. *J. Am. Chem. Soc.* **2008**, *130*, 5940–5946.
121. Konermann, L.; Ahadi, E.; Rodriguez, A. D.; Vahidi, S. Unraveling the Mechanism of Electrospray Ionization. *Anal. Chem.* **2013**, *85*, 2–9.
122. Qian, H.; Zhu, Y.; Jin, R. Size-Focusing Synthesis, Optical and Electrochemical Properties of Monodisperse Au₃₈(SC₂H₄Ph)₂₄ Nanoclusters. *ACS Nano* **2009**, *3*, 3795–3803.
123. Qian, H.; Zhu, Y.; Jin, R. Atomically precise gold nanocrystal molecules with surface plasmon resonance. *Proc. Natl. Acad. Sci.* **2012**, *109*, 696–700.
124. Jeyabharathi, C.; Senthil Kumar, S.; Kiruthika, G. V. M.; Phani, K. L. N. Aqueous CTAB-Assisted Electrodeposition of Gold Atomic Clusters and Their Oxygen Reduction Electrocatalytic Activity in Acid Solutions. *Angew. Chem., Int. Ed.* **2010**, *49*, 2925–2928.
125. Yang, X.; Gan, L.; Zhu, C.; Lou, B.; Han, L.; Wang, J.; Wang, E. A dramatic platform for oxygen reduction reaction based on silver nanoclusters. *Chem. Commun.* **2014**, *50*, 234–236.
126. Negishi, Y.; Chaki, N. K.; Shichibu, Y.; Whetten, R. L.; Tsukuda, T. Origin of Magic Stability of Thiolated Gold Clusters: A Case Study on Au₂₅(SC₆H₁₃)₁₈. *J. Am. Chem. Soc.* **2007**, *129*, 11322–11323.
127. Fu, F.; Xiang, J.; Cheng, H.; Cheng, L.; Chong, H.; Wang, S.; Li, P.; Wei, S.; Zhu, M.; Li, Y. A Robust and Efficient Pd₃ Cluster Catalyst for the Suzuki Reaction and Its Odd Mechanism. *ACS Catal.* **2017**, *7*, 1860–1867.
128. Laborda, F.; Bolea, E.; Jiménez-Lamana, J. Single Particle Inductively Coupled Plasma Mass Spectrometry: A Powerful Tool for Nanoanalysis. *Anal. Chem.* **2014**, *86*, 2270–2278.
129. Fabricius, A.-L.; Duyster, L.; Meermann, B.; Ternes, T. A. ICP-MS-based characterization of inorganic nanoparticles—sample preparation and off-line fractionation strategies. *Anal. Bioanal. Chem.* **2014**, *406*, 467–479.
130. Meermann, B.; Sperling, M. Hyphenated techniques as tools for speciation analysis of metal-based pharmaceuticals: developments and applications. *Anal. Bioanal. Chem.* **2012**, *403*, 1501–1522.

131. Meermann, B.; Nischwitz, V. ICP-MS for the analysis at the nanoscale – a tutorial review. *J. Anal. At. Spectrom.* **2018**, *33*, 1432–1468.
132. Zhang, X.; Wu, Z.; Zhang, X.; Li, L.; Li, Y.; Xu, H.; Li, X.; Yu, X.; Zhang, Z.; Liang, Y.; Wang, H. Highly selective and active CO₂ reduction electrocatalysts based on cobalt phthalocyanine/carbon nanotube hybrid structures. *Nat. Commun.* **2017**, *8*, 14675.
133. Negishi, Y.; Matsuura, Y.; Tomizawa, R.; Kurashige, W.; Niihori, Y.; Takayama, T.; Iwase, A.; Kudo, A. Controlled Loading of Small Au_n Clusters (*n* = 10–39) onto BaLa₄Ti₄O₁₅ Photocatalysts: Toward an Understanding of Size Effect of Cocatalyst on Water-Splitting Photocatalytic Activity. *J. Phys. Chem. C* **2015**, *119*, 11224–11232.
134. Larner, F.; Rehkämper, M. Evaluation of Stable Isotope Tracing for ZnO Nanomaterials—New Constraints from High Precision Isotope Analyses and Modeling. *Environ. Sci. Technol.* **2012**, *46*, 4149–4158.
135. Laycock, A.; Stolpe, B.; Römer, I.; Dybowska, A.; Valsami-Jones, E.; Lead, J. R.; Rehkämper, M. Synthesis and characterization of isotopically labeled silver nanoparticles for tracing studies. *Environ. Sci.: Nano* **2014**, *1*, 271–283.
136. Degueldre, C.; Favarger, P. Y. Colloid analysis by single particle inductively coupled plasma-mass spectroscopy: a feasibility study. *Colloids Surf. A Physicochem. Eng. Asp.* **2003**, *217*, 137–142.
137. Meermann, B.; Wichmann, K.; Lauer, F.; Vanhaecke, F.; Ternes, T. A. Application of stable isotopes and AF4/ICP-SFMS for simultaneous tracing and quantification of iron oxide nanoparticles in a sediment–slurry matrix. *J. Anal. At. Spectrom.* **2016**, *31*, 890–901.
138. Meermann, B. Field-flow fractionation coupled to ICP–MS: separation at the nanoscale, previous and recent application trends. *Anal. Bioanal. Chem.* **2015**, *407*, 2665–2674.
139. Liang, J.-X.; Lin, J.; Yang, X.-F.; Wang, A.-Q.; Qiao, B.-T.; Liu, J.; Zhang, T.; Li, J. Theoretical and Experimental Investigations on Single-Atom Catalysis: Ir1/FeOx for CO Oxidation. *J. Phys. Chem. C* **2014**, *118*, 21945–21951.
140. Liang, J.-X.; Yang, X.-F.; Wang, A.; Zhang, T.; Li, J. Theoretical investigations of non-noble metal single-atom catalysis: Ni1/FeOx for CO oxidation. *Catal. Sci. Technol.* **2016**, *6*, 6886–6892.
141. Li, F.; Li, Y.; Zeng, X. C.; Chen, Z. Exploration of High-Performance Single-Atom Catalysts on Support M1/FeOx for CO Oxidation via Computational Study. *ACS Catal.* **2015**, *5*, 544–552.
142. Lou, Y.; Zheng, Y.; Li, X.; Ta, N.; Xu, J.; Nie, Y.; Cho, K.; Liu, J. Pocketlike Active Site of Rh₁/MoS₂ Single-Atom Catalyst for Selective Crotonaldehyde Hydrogenation. *J. Am. Chem. Soc.* **2019**, *141*, 19289–19295.
143. Stamatakis, M.; Vlachos, D. G. Unraveling the Complexity of Catalytic Reactions via Kinetic Monte Carlo Simulation: Current Status and Frontiers. *ACS Catal.* **2012**, *2*, 2648–2663.
144. Stamatakis, M. Kinetic modelling of heterogeneous catalytic systems. *J. Phys. Condens. Matter* **2014**, *27*, 013001.
145. Kopač, D.; Likozar, B.; Huš, M. Catalysis of material surface defects: Multiscale modeling of methanol synthesis by CO₂ reduction on copper. *Appl. Surf. Sci.* **2019**, *497*, 143783.

146. Kopač, D.; Huš, M.; Ogrizek, M.; Likozar, B. Kinetic Monte Carlo Simulations of Methanol Synthesis from Carbon Dioxide and Hydrogen on Cu(111) Catalysts: Statistical Uncertainty Study. *J. Phys. Chem. C* **2017**, *121*, 17941–17949.
147. Huš, M.; Dasireddy, V. D. B. C.; Strah Štefančič, N.; Likozar, B. Mechanism, kinetics and thermodynamics of carbon dioxide hydrogenation to methanol on Cu/ZnAl₂O₄ spinel-type heterogeneous catalysts. *Appl. Catal., B* **2017**, *207*, 267–278.